Accuracy of Linearized Reflection Coefficients for Converted Waves in Anisotropic Media

Ellen de N.S. Gomes,CPGF/ufpa,ellensg@ufpa.br, Jessé C. Costa,ufpa,jesse@ufpa.br, João S. Protázio, ufpa,protazio@ufpa.br, Ivan de Araújo Simões Filho, UNICAMP/ANP, iasf@anp.gov.br.

Summary

The reflection coefficients at a planar interface separating two anisotropic media have a highly nonlinear dependence on the elastic parameters and densities of both media. Linear approximations on the elastic parameters for the qP wave reflectivity are more convenient for AVO/AVD analysis. We present a simple derivation of linearized approximations for convertd waves reflectivity for weak impedance contrast and general weak anisotropy. The derivation is simplified by writing the solution of Zoeppritz equations explicitly in terms of impedance and polarization matrices. The linear approximations for converted waves reflection coefficients are very close to the exact results for incidence angles up to 30 degrees considering moderate impedance contrast and mild anisotropy. Only the linear approximations of converted waves reflection coefficients are sensitive to fractures strike and dip.

Introduction

AVO/AVD analysis extended to anisotropic models could provide, besides some lithological parameters and the prognostic of fluid content, a way to infer principal directions of reservoir permeability associated to microfractures at a scale below the resolution limit of seismic waves.

Several approximations for the reflection coefficients of a reflected qP wave from an incident qP wave, R_{qPqP}, have been proposed. Assuming weak impedance contrast, weak anisotropy and higher symmetry the main contributions are Thomsen (1986, 1993) and Banik (1987). For arbitrary impedance contrast and weak anisotropy Zillmer et al. (1997) presented a nonlinear approximation on the elastic parameters. Vavryčuk & Pšenčik (1998) presented an explicit linear approximation for R_{qPqP} for media with weak impedance contrast and weak anisotropy. Approximations for converted waves reflection coefficients for qP incidence are derived by Vavryčuk (1999) assuming weak impedance contrast and weak anisotropy, though no explicit formula on the elastic parameters which are convenient for AVO/AVD analysis were presented. Gomes(1999) and Gomes et al.(2001) and more recently Jílek(2001) arrived at similar expressions to the ones presented here.

We present explicit linearized approximations for reflection coefficients of converted waves for qP incidence at an interface across two weak anisotropic media with weak impedance contrast. In contrast to R_{qPqP}, the approximations of converted waves depend on fractures strike and dip and are accurate for incidence angles under 30 degrees.

Zoeppritz Equations

Consider two arbitrary anisotropic media separated by a plane interface, $x_3 = 0$. The incident and reflected waves propagate at the upper medium and the transmitted waves propagate through the lower medium. Assuming that the plane wave approximation is locally valid, the incident and scattered waves at the interface can be written as

$$\mathbf{u}_\alpha(\mathbf{x},t) = A_\alpha\, \mathbf{n}_\alpha \exp i\omega\left(\mathbf{s}_\alpha.\mathbf{x} - t\right) \qquad (1)$$

where $\mathbf{u}_\alpha$ is the displacement vector; $\mathbf{n}_\alpha$ is the polarization unit vector; A_α is the wave amplitude; $\mathbf{s}_\alpha$ is the slowness vector; $\mathbf{x}$ is the observation position vector, t is the time and ω is the angular frequency. The subscript α labels the wave types qP, qS_1 and qS_2.

Considering the traction and displacement continuous across the interface we arrive at the Zoeppritz equations

$$\begin{aligned} \mathbf{N}_I\,\mathbf{i} + \mathbf{N}_R\,\mathbf{r} &= \mathbf{N}_T\,\mathbf{t} \\ \mathbf{Z}_I\,\mathbf{i} + \mathbf{Z}_R\,\mathbf{r} &= \mathbf{Z}_T\,\mathbf{t} \end{aligned}, \qquad (2)$$

where $N_{i\alpha} = n_{i\alpha}$; $Z_{i\alpha} = c_{3ijk}\, s_{k\alpha}\, n_{j\alpha}$ and c_{ijkl} are the components of the medium elastic tensor. The matrices $\mathbf{N}_I$, $\mathbf{N}_R$, $\mathbf{N}_T$, $\mathbf{Z}_I$, $\mathbf{Z}_R$ e $\mathbf{Z}_T$ are the polarization and impedance matrices for the incident, reflected and transmitted waves respectively and, their correspondent amplitudes are represented by the vectors $\mathbf{i} = i_\alpha$, $\mathbf{r} = r_\alpha$ and $\mathbf{t} = t_\alpha$. The solution of the linear system (2) for the reflected and transmitted amplitudes in terms of impedance and polarization matrices is

$$\begin{aligned} \mathbf{r} \equiv \mathbf{R}\,\mathbf{i} &= \left(\mathbf{Z}_R - \mathbf{Z}_T\mathbf{N}_T^{-1}\mathbf{N}_R\right)^{-1}\left(\mathbf{Z}_I - \mathbf{Z}_T\mathbf{N}_T^{-1}\mathbf{N}_I\right)\mathbf{i}, \\ \mathbf{t} \equiv \mathbf{T}\,\mathbf{i} &= -\left(\mathbf{Z}_T - \mathbf{Z}_R\mathbf{N}_R^{-1}\mathbf{N}_T\right)^{-1}\left(\mathbf{Z}_I - \mathbf{Z}_R\mathbf{N}_R^{-1}\mathbf{N}_I\right)\mathbf{i}. \end{aligned} \qquad (3)$$

The matrices $\mathbf{R}$ and $\mathbf{T}$ contain all the reflected and transmission coefficients for each wave type. Specifically, the reflection coefficients for qP incidence R_{qPqP}, R_{qS_1qP} and R_{qS_2qP} form the first column of $\mathbf{R}$:

$$\mathbf{R} = \left[R_{\alpha\beta}\right] = \begin{bmatrix} R_{qPqP} & R_{qPqS_1} & R_{qPqS_2} \\ R_{qS_1qP} & R_{qS_1qS_1} & R_{qS_1qS_2} \\ R_{qS_2qP} & R_{qS_2qS_1} & R_{qS_2qS_2} \end{bmatrix}. \qquad (4)$$

Linearization

The solution of Zoeppritz equations in terms of polarization and impedance matrices are very useful for deriving linearized expressions for the reflection coefficients. We consider an arbitrary homogeneous isotropic medium as a reference background and define all the perturbations on this isotropic background. The first order perturbation of reflection and

transmission matrices is derived from (3) and obeys the system of equations:

$$\begin{matrix}\left(\widetilde{\mathbf{Z}}_R-\widetilde{\mathbf{Z}}_T\,\widetilde{\mathbf{N}}_T^{-1}\,\widetilde{\mathbf{N}}_R\right)\delta\mathbf{R}=2\left(\Delta\mathbf{Z}-\widetilde{\mathbf{Z}}_T\,\widetilde{\mathbf{N}}_T^{-1}\Delta\mathbf{N}\right)\\ \left(\widetilde{\mathbf{Z}}_T-\widetilde{\mathbf{Z}}_R\,\widetilde{\mathbf{N}}_R^{-1}\,\widetilde{\mathbf{N}}_T\right)\delta\mathbf{T}=-2\left(\Delta\mathbf{Z}-\widetilde{\mathbf{Z}}_R\,\widetilde{\mathbf{N}}_R^{-1}\Delta\mathbf{N}\right)\end{matrix}, \quad (5)$$

where the matrices $\widetilde{\mathbf{Z}}_k$ and $\widetilde{\mathbf{N}}_k$, with $k = I, R, T$, are the impedance and polarization matrices associated to the incident, reflected and transmitted waves at the isotropic background; $\Delta\mathbf{N}=(\delta\mathbf{N}_T-\delta\mathbf{N}_I)/2$ and $\Delta\mathbf{Z}=(\delta\mathbf{Z}_T-\delta\mathbf{Z}_I)/2$ are the average contrast for the polarization and impedance matrices across the upper and lower medium; $\delta\mathbf{Z}_I$, $\delta\mathbf{Z}_T$ and $\delta\mathbf{N}_I$, $\delta\mathbf{N}_T$ are the perturbations for the impedance and polarization matrices at the upper and lower medium, respectively, relative to the isotropic background. In order to apply equation (5), the polarizations of the shear waves in the reference medium must be specified, we choose the SV and SH directions as our reference for shear wave polarizations at the background medium. With these choices linear approximations for qP reflectivity are presented below. In these expressions we use the reduced notation for elastic tensors. The elastic tensors on the top and bottom medium are written as $C_{ij}=C_{ij}^{iso}+\delta C_{ij}$, where C_{ij}^{iso} is an isotropic part of each elastic tensor specified independently for each medium and $\Delta C_{ij}=\left(\delta C_{ij}^{I}-\delta C_{ij}^{T}\right)/2$; ρ is the density and G is the shear modulus, $\kappa=\beta/\alpha$ is the ratio between S-wave and P-wave velocities in the reference isotropic background. The linearized approximation for R_{SVP} is

$$\begin{aligned}\delta R_{SVP}=\delta R_{SVP}^{(ISO)}+\frac{1}{2\rho\,\alpha^2\,\eta(\theta)}\Big\{\big[2\big(\Delta C_{11}\cos^4\varphi+\\ \Delta C_{22}\,\sin^4\varphi+2(\Delta C_{16}\cos^2\varphi+\Delta C_{26}\,\sin^2\varphi)\sin 2\varphi\big)+\\ \Delta(C_{12}+2C_{66})\sin^2 2\varphi\big]\sin^3\theta+\big[2\big(\Delta(C_{13}+2C_{55})\cos^2\varphi+\\ \Delta(C_{23}+2C_{44})\,\sin^2\varphi\big)-4\,(\Delta C_{55}\cos^2\varphi+\Delta C_{44}\,\sin^2\varphi)+\\ 2\,\Delta C_{36}\sin 2\varphi\big]\sin\theta\cos 2\theta+\frac{1}{\kappa\,K(\theta)}\Big\{\big[2\big(\Delta C_{15}\cos^3\varphi+\\ \Delta C_{24}\sin^3\varphi\big)+\big(\Delta(C_{25}+2C_{46})\,\sin\varphi+\Delta(C_{14}+2C_{56})\\ \cos\varphi\big)\sin 2\varphi\big]\sin^2\theta\big(2\kappa\omega(\theta)-1\big)+2\big[\Delta C_{34}\sin\varphi\;+\\ \Delta C_{35}\cos\varphi\big]\cos\theta\big[\cos\theta-2K(\theta)\,\omega(\theta)\big]-\\ \Delta C_{33}\,\sin 2\theta\cos\theta\kappa K(\theta)+2\big[\Delta C_{55}\,\cos^2\varphi+\Delta C_{44}\,\sin^2\varphi+\\ \Delta C_{45}\sin 2\varphi\big]\,\sin 2\,\theta\,(\kappa^2\sin^2\theta-K^2(\theta))\Big\}\Big\},\end{aligned} \quad (6)$$

the approximation for R_{SHP} is

$$\begin{aligned}\delta R_{SHP}=\frac{1}{2\rho\,\alpha^2\,K(\theta)}\Big\{\frac{1}{\kappa}\Big\{2\big[\Delta(C_{24}-2C_{56})\cos\varphi\,\sin^2\varphi\;-\\ \Delta(C_{15}-2\,C_{46})\cos^2\varphi\,\sin\varphi+\Delta C_{14}\cos^3\varphi-\Delta C_{25}\sin^3\varphi\big]\\ \sin^2\theta+\big[\Delta(C_{44}-C_{55})\sin 2\varphi+2\Delta C_{45}\cos 2\varphi\big]\;\sin\;2\theta+\\ 2\big[\Delta C_{34}\;\cos\varphi-\Delta C_{35}\;\sin\varphi\big]\cos^2\theta\Big\}-\frac{1}{\eta(\theta)}\\ \Big\{\big[(\Delta C_{22}\sin^2\varphi-\Delta C_{11}\cos^2\varphi)\sin 2\varphi+\Delta\,(C_{12}+2C_{66})\\ \sin 2\varphi\,\cos 2\varphi+2\Delta C_{16}\cos^2\varphi(\cos^2\varphi-3\sin^2\varphi)+\\ 2\,\Delta C_{26}\sin^2\varphi\,(3\,\cos^2\varphi-\sin^2\varphi)\;\big]\sin^3\theta\;+\\ 2\,\big[\,\Delta\,(C_{14}+2C_{56})\,\cos\varphi\,(\cos^2\varphi-2\,\sin^2\varphi)+\\ \Delta(C_{25}+2C_{46})\sin\varphi\,(2\cos^2\varphi-\sin^2\varphi)+\\ 3(\Delta C_{24}\sin\varphi-\Delta C_{15}\cos\varphi)\sin\varphi\,\cos\varphi\big]\cos\theta\sin^2\theta+\\ \big[(\Delta\,(C_{23}+2C_{44})-\Delta\,(C_{13}+2C_{55}))\sin 2\varphi\;+\\ 2\,\Delta(C_{36}+2C_{45})\,\cos 2\,\varphi\big]\cos^2\theta\,\sin\theta\;+\\ 2\,\big[\,\Delta C_{34}\cos\,\varphi-\,\Delta C_{35}\sin\,\varphi\,\big]\cos^3\theta\,\Big\}\Big\}\end{aligned}, \quad (7)$$

where φ is azimuth angle, θ is incidence angle; $K(\theta)=\sqrt{1-\kappa^2\sin^2\theta}$ is the cosine of the reflection angle of the S wave, $\omega(\theta)=\kappa\sin^2\theta+K(\theta)\cos\theta$ and $\eta(\theta)=K(\theta)+\kappa\cos\theta$. The isotropic part of the converted SV wave reflection coefficient is

$$\delta R_{SVP}^{(ISO)}=\frac{\sin\theta}{K(\theta)}\left[-\frac{\Delta\rho}{\rho}+2\kappa\,(\kappa\sin^2\theta-K(\theta)\,\cos\theta)\,\frac{\Delta G}{G}\right],$$

where $\Delta\rho$ and ΔG are the half difference between densities and shear moduli of the isotropic part of each medium. The linearized approximation for R_{PP} is similar to the one presented by Vavryčuk & Pšenčik (1998) and is not presented here.

Numerical Examples

To illustrate the precision of the linear approximations we present an example of the reflection coefficients of an isotropic medium over a transversally isotropic medium with symmetry axis at the direction 60 degrees of azimuth and dipping 30 degrees relative to the interface. The isotropic top medium has density 2.20g/cm^3, P wave velocity 4.23km/s and shear wave velocity 2.73km/s. The unrotated ortorrombic medium has density 2.6g/cm^3 and its elastic tensor in reduced notation is

$$C = \begin{bmatrix} 66.66 & 39.42 & 19.62 & 0.00 & 0.00 & 0.00 \\ 39.42 & 39.96 & 39.49 & 0.00 & 0.00 & 0.00 \\ 19.62 & 39.49 & 66.66 & 0.00 & 0.00 & 0.00 \\ 0.00 & 0.00 & 0.00 & 10.94 & 0.00 & 0.00 \\ 0.00 & 0.00 & 0.00 & 0.00 & 23.52 & 0.00 \\ 0.00 & 0.00 & 0.00 & 0.00 & 0.00 & 10.94 \end{bmatrix}$$

in GPa. Although the contrast of impedance at normal incidence is weak the anisotropy is not so. For the computation of (6) and (7) the isotropic part of the bottom medium has the same density and $\rho\alpha^2 = C_{33}$ and $\rho\beta^2 = C_{55}$. The isotropic background has the average density and average P-wave and S-wave velocity of top and bottom isotropic parts. Figure 1 to 6 show the exact value, the linearized approximation and the absolute error for R_{SVP} and R_{SHP} also for incidence angles up to 40 degrees. The exact values where computed solving the system of equations (3). These stereograms clearly show that reflection coefficients of converted waves are sensitive to the symmetry axis orientation. As a consequence, only converted waves reflection coefficients are sensitive to the strike and dip of a system of parallel fractures.

Other tests not presented here show that the approximations degrades more quickly for increasing impedance contrast across the interface than for increasing anisotropy of the bottom medium. Also if the top medium is anisotropic and do not present azimuthal symmetry R_{SVP} and R_{SHP} may not be so close to R_{qS_1qP} and R_{qS_2qP}. We need to known the polarizations of qS_1 and qS_2 waves to have a better approximation.

Conclusions

Linear approximations of the reflection coefficients for qP incidence were derived from the solutions of Zoeppritz equations written in a partitioned form using polarization and impedance matrices. The linear approximations for the reflection coefficients of converted waves are accurate for incidence angles smaller than 30 degrees for weak anisotropy and weak impedance contrast across the interface. In contrast to R_{PP} coefficient, which is sensitive only to the fractures strike, convert waves reflection coefficients are sensitive to fractures dip also.

References

Banik**,** N**.** C**.,** 1987. An effective anisotropy parameter in transversely isotropic media. Geophysics, 52, 1654-1664.

Gomes, E., 1999. Reflectivity of P waves in anisotropic media (in Portuguese). Master Thesis. Department of Mathematics of Universidade Federal do Pará, Brazil.

Gomes, E., Protázio, J.S., Costa, J. Simões-Filho, I.A., 2001. Linearization of qP wave reflection coefficients in anisotropic media(in Portuguese). Accepted for publication in the Brazilian Journal of Geophysics.

Jílek, P., 2001. Converted PS-wave reflection coefficients in weakly anisotropic media. Accepted for publication in Pure and Applied Geophysics.

Thomsen**,** L., 1986. Weak elastic anisotropy. Geophysics, 51, 1954-1966.

Thomsen, L., 1993. Weak elastic anisotropic reflection. In Castagna, J. P. and Backus, M. M. Eds. Offset-dependent reflectivity-theory and practice AVO analysis: Soc. Exp. Geophys. 103-111.

Vavryčuk, V., & Pšenčik, I., 1998. PP-wave reflection coefficients in weakly anisotropic media: Geophysics, 63, 2129-2141.

Vavryčuk, V., 1999. Weak-contrast reflection/transmission coefficients in weakly anisotropic elastic media. Geophys. J. Int., 138, 553-562.

Zillmer, M., Gajewski, D. & Kashtan, B. M., 1997. Reflection coefficients for weak anisotropic. Geophys. J. Intern., 129, 389-398.

Acknowledgments

The authors acknowledge the financial support of the FINEP/CNPq/Pronex in Reservoir Engineering and Prof. Ivan Pšenčik for the fruitful discussions.

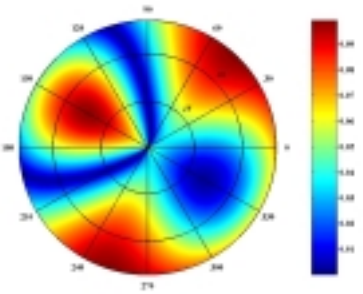

Figure 1: Stereogram for the exact R_{qS1qP}

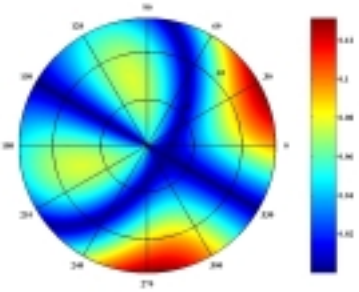

Figure 4: Stereogram for the exact R_{qS2qP} .

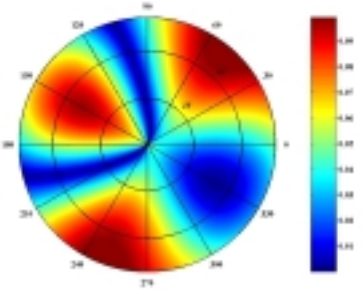

Figure 2: Stereogram for the linearized R_{SVP} .

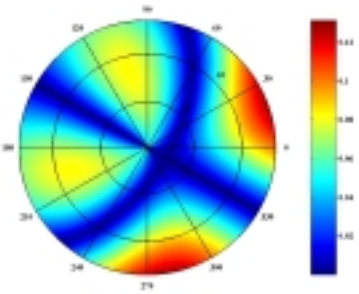

Figure 5: Stereogram for the linear approximation of R_{SHP} .

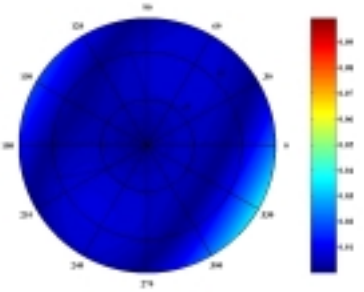

Figure 3: Stereogram for the absolute error of R_{SVP} linear approximation.

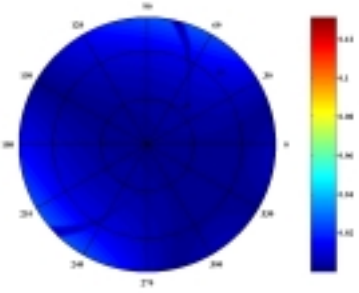

Figure 6: Stereogram for the absolute error of the R_{SHP} linear approximation.

Converted Waves from Gas Hydrates: Constraints on the shear velocity structure of shallow sediments in Oregon Continental Margin

Mrinal K. Sen, Chengshu Wang, and Nathan Bangs, Institute for Geophysics, The University of Texas at Austin, USA

Abstract

Gas hydrates are frozen methane gas that can be found along most continental margins worldwide. Estimates of elastic properties of hydrate-bearing sediments are essential to evaluating the gas-content. Robust est1imates of these parameters can be obtained by pre-stack inversion. However, the conventional streamer data cannot constrain the shear wave velocity well; a property that is essential to identification and quantification of gas. Here we report on the first observation of converted waves from hydrate-bearing sediments recorded on multi-component ocean bottom seismometers deployed during a field survey across the Oregon continental margin. We employ plane wave processing including interactive P and S wave velocity analysis of the data to obtain robust estimates of these parameters. The results are extremely useful in characterization of gas hydrates in continental margins.

Introduction

Academic institutions have been using ocean bottom seismometers (OBS) for deep-water seismic refraction surveys for over two decades now. Although OBSs record all four components (pressure, vertical and two horizontal components), only the hydrophone and vertical geophone data have been routinely used. Unlike OBS surveys, where only a sparse set of receivers is used in a typical study, 4C geophones are deployed at the seafloor at dense spatial sampling (typically 25m) along a cable to record converted waves, also called C waves (Thomsen 1999). PS surveys using OBCs yield images of the sub sea structure at similar resolution and quality as traditional marine P-wave reflection surveys. For hydrocarbon exploration, C waves are proving to be particularly powerful in the illumination of gas and sub-gas structures (S waves travel almost undisturbed through gas zones; e.g., Granli et al., 1999) and for a lithologic identification of gas reservoirs based on amplitudes (PP bright spots with only moderate PS arrivals, e.g., Zaengle and Frasier, 1993). Processing and interpretation techniques of OBS data are still in their early stages of development even in the hydrocarbon industry and the range of questions that can be addressed with OBC surveys will most likely grow in the near future.

The objective of this paper is two-fold. First we briefly review methods for processing of multi-component OBS and OBC data in the plane wave domain and then present results from analysis of ocean bottom seismometer data collected at the Oregon continental margin. The Oregon continental margin experiment was carried out to study the gas-hydrate distribution and to estimate free gas content of the shallow sediments in the area. Answers to many of the questions related to the formation and distribution of gas hydrates depend on the robust measurement of S-wave velocity (Vs). New rock-physics studies of gas hydrate-bearing sediments emphasize the importance of Vs for gas hydrate quantification. We are able to obtain robust estimates of Vs from the OBS data from the Oregon continental margin and can thus make estimates of gas-content in the hydrated sediments and within the free gas zone.

Determination of Vp from normal moveout of hydrophone common mid-point (CMP) gathers is fairly a standard practice now. The estimation of Vs is not trivial. The common procedure is outlined below:

- Get an estimate of Vp-Vs ratio γ from normal incidence PP and PS times. Note that normal incidence PS amplitude is zero, and therefore, PS normal incidence times are extrapolated from oblique incident arrivals.
- Use γ to compute conversion points and sort PS gathers into common conversion point (CCP) gathers.
- Apply an rms stacking velocity analysis (with non-hyperbolic terms) of CCP gathers.

Like the CMPs, CCPs also resemble synthetic aperture and thus the effect of lateral heterogeneity is minimized. Note, however, that the CCP depends on the choice of γ and the NMO correction using rms velocities introduces another level of approximation. Therefore, in addition to using the conventional approach described here, we employ τ-p interactive PS velocity analysis of common receiver gathers along strike line (nearly 1D structure) to obtain Vs interval velocity. The τ-p trajectory of the converted waves is given by:

$$\tau(p) = \Delta z \left(q_P + q_S\right), \qquad (1)$$

where q_P and q_S are the vertical slownesses of the P and S waves respectively and Δz is the layer thickness. For an isotropic medium, Eq. (1) reduces to the following form

$$\tau(p) = \tau_P^0 \left(1 - p^2 v_p^2\right)^{\frac{1}{2}} + \tau_s^0 \left(1 - p^2 v_s^2\right)^{\frac{1}{2}} . \qquad (2)$$

Note that extension of τ-p velocity analysis to include anisotropy is fairly straightforward. In a transversely isotropic medium, the vertical slowness can be computed analytically from the solution of a quadratic

equation. The vertical slowness for a general azimuthally anisotropic medium can be computed numerically.

Having obtained the velocity models, we can apply pre-stack time or depth migration based on kirchhoff plane-wave migration. We can also apply pre-stack waveform inversion of PP and PS data in which we use a reflectivity method for the calculation of synthetic seismograms and a very fast simulated annealing (VFSA) for optimization.

Gas Hydrates and 3D streamer/OBS survey in the Oregon margin

Gas hydrates are frozen methane gas that forms at specific pressure and temperature conditions. They are found in the marine sediments along continental margins worldwide. They have the economic potential of being tapped as a fuel source and also have the potential as a "greenhouse" agent after being freed into the atmosphere. In seismic sections, the occurrence of the base of gas hydrates, in some areas, is often marked by a bright amplitude reflection. Such reflections follow the sea floor topography and are called bottom-simulating reflectors (BSR). The BSRs have reverse polarity with respect to the sea-floor reflection, and in a common shot or CDP gather, the amplitude increases with offset. Direct sampling of gas hydrates is difficult. This is partly due to the fact that under normal surface pressure and temperature conditions, gas hydrates vigorously dissociate before reaching the surface. Drilling of BSRs proved to be even more difficult because of the risk of releasing free gas underneath BSR. ODP Leg 141 was the first attempt to intentionally penetrate BSR (Bangs et al., 1993). However, seismic waveform data can be analyzed to infer elastic properties of hydrate-bearing sediments above and normal sediments below BSR. Recently Xia et. al. (2000) applied a pre-stack inversion of streamer data and obtained profiles of elastic properties. However, since only P wave data were used, good prior knowledge of S-wave velocity structure was required.

In the summer of 2000, scientists from UTIG (Bangs, Nakamura) and University of Oregon (Trehu) conducted a 3D streamer and OBS survey in the active margin hydrate system of Oregon continental margin. The map of the survey area and the lines are shown in Fig 1 (upper panel); 20 OBS were deployed at the seafloor. Preliminary analysis of the 3D data were reported by Bangs et. al. (2000) at the AGU fall meeting; excellent images of the BSR were obtained. Figure 1 (lower panel) shows a 2D profile from the 3D volume on which OBS data are superimposed. Notice the excellent correlation between OBS and streamer data – the BSR matches well in the two data sets. As an example, we show the OBS gathers for the hydrophone, vertical and radial geophones. We were able to correlate the converted wave arrivals in the radial component with P wave arrivals in the hydrophone data at all OBSs. The data were then plane wave transformed and interactive velocity analysis was carried out to obtain both P and S wave velocities. As an example, we show the NMO corrected OBS gathers from location 101 and the corresponding Vp and Vs profiles. The zone below BSR shows a sharp decrease in Vp with almost no change in Vs indicating the presence of free gas. The Vp AND Vs values thus derived were interpolated and a map of high resolution Vp and Vs were obtained. These were then used in the estimation of free gas content in the hydrated sediments. More detailed joint PP and PS pre-stack inversion is also being carried out.

Conclusions

In this paper we report on the observation of converted waves from hydrated sediments in the Oregon continental margin recorded by the ocean bottom seismometers. High quality recordings enabled us to identify both PPS and PSS arrivals on the horizontal seismograms. They were used to estimate shear wave velocity structure in the sediments. Thus we are able to obtain better estimates of the gas concentration within the hydrated sediments.

References

Bangs, N. L., D. W. Sawyer, and X. Golovechenko, 1993, Free gas at the base of gas hydrate zone in the vicinity of Chile triple junction, Geology, 21, 905-908.

Granli, J. R., B. Arnsten, A. Sollid, and E. Hilde, 1999, Imaging through gas-filled sedminents using marine shear-wave data, Geophysics, 64(3), 668-677.

Thomsen, L., 1999, Converted-wave reflection seismolgy over inhomogeneous, anisotropic media, Geophysics, 64(3), 678-690.

Acknowledgments

This research was supported by the National Science Foundation Ocean Sciences – Ocean Drilling Program

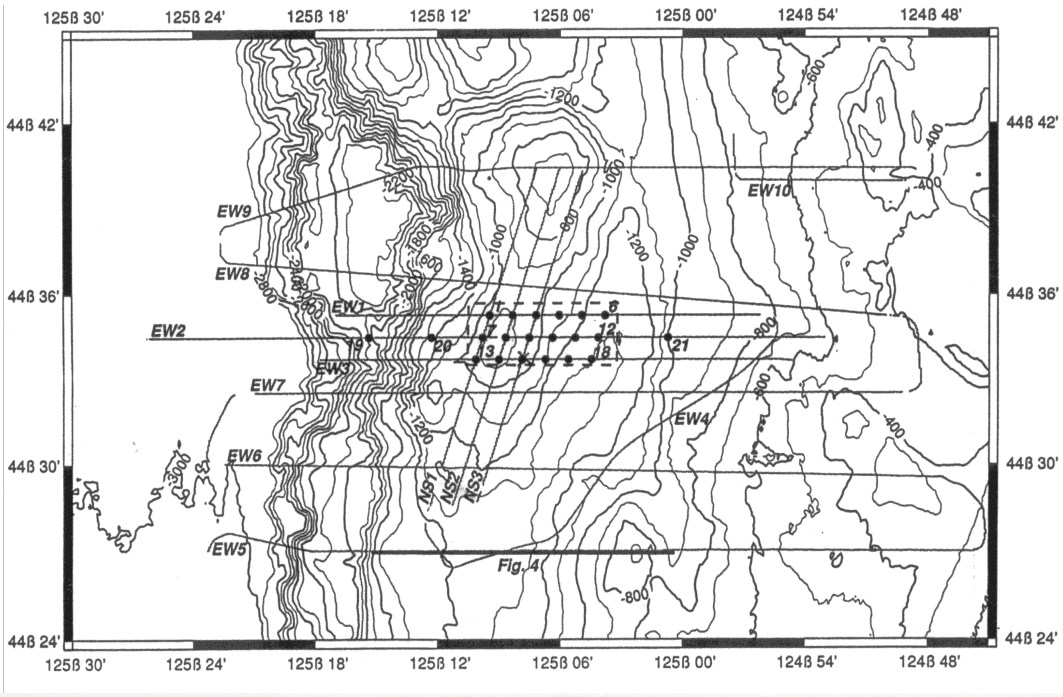

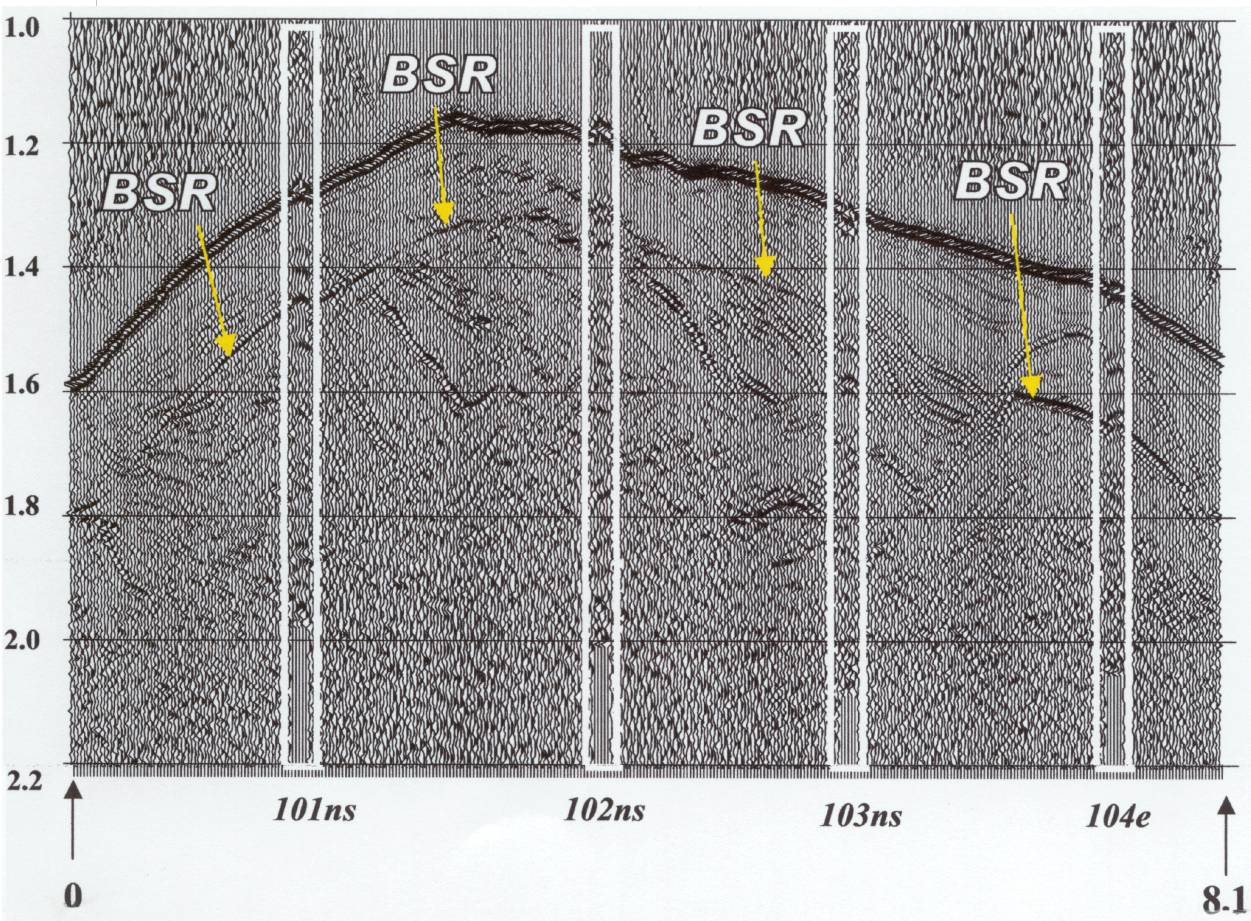

Figure 1 (upper) Bathymetric map showing regional lines, OBS locations (numbered dots) , and the location of the 3D seismic survey (red dashed box)
(lower) A 2D seismic section on which OBS near offset traces have been superimposed. The BSR can be clearly seen.

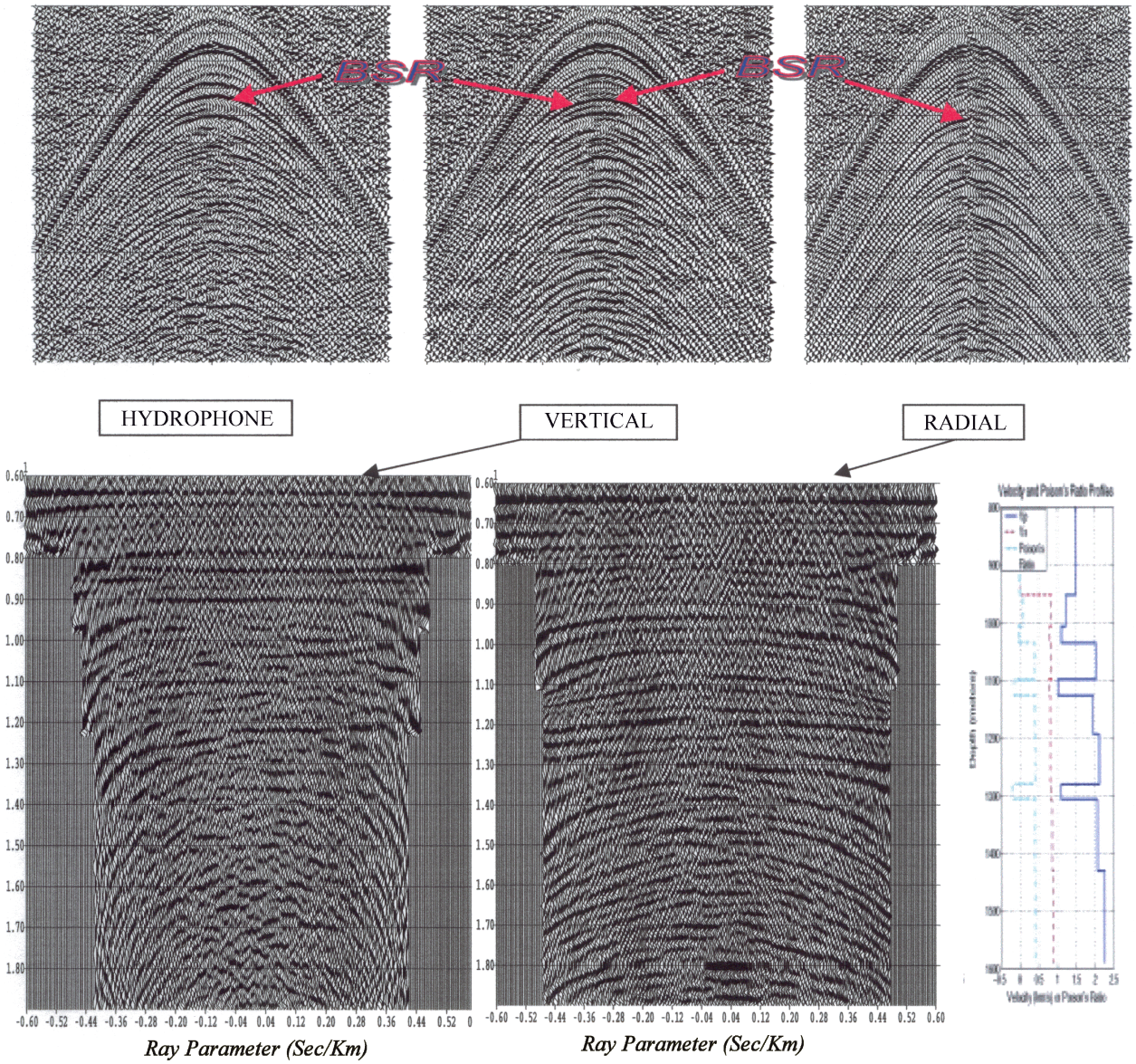

Figure 2: (Upper panel) OBS records from location 101 – pressure, vertcal, and horizontal geophones. The BSR has been marked at both Z and R components.
(lower panel) NMO corrected Vertical and tadial tau-p gathers and the corresponding velocity models.

Detecção de fraturas através de AVO/AVD de ondas qP e suas convertidas em meios anisotrópicos

Ellen de N.S. Gomes,CPGf/UFPA, ellensg@ufpa.br*
Jessé C. Costa,Depto de Física/UFPA, jesse@ufpa.br
João S. Protázio, Depto de Matemática/UFPA, protazio@ufpa.br
Ivan de Araújo Simões Filho,ANP/UNICAMP,iasf@anp.gov.br

Abstract
We investigate the detection of fractures orientation through AVO/AVD analysis of qP and its converted waves. Linearized approximations for the reflection coefficients are used to invert exact multiazimuth reflection coefficients for density and elastic parameters contrast. Though converted waves are sensitive to fractures strike and dip, the SVD analysis of the linearized inversion shows that qP reflection data is necessary to recover the fractures orientation.

Introdução
As propriedades elásticas das rochas na subsuperfície podem ser estimadas através do estudo das amplitudes das ondas refletidas utilizando-se análise da amplitude versus afastamento (AVO) e amplitude versus direção (AVD). Essas análises têm sido importantes no prognóstico de contrastes litológicos ou de conteúdo de fluidos das formações. Em meios com fraturamento pode-se, por exemplo, determinar a orientação de planos de fratura que em geral indicam a direção de maior permeabilidade que é essencial à caracterização de reservatórios de hidrocarbonetos. Para modelos interpretativos que admitem anisotropia as expressões analíticas dos coeficientes de reflexão dependem de forma não linear dos parâmetros elásticos do meio, o que torna a análise AVO/AVD muito complexa. Devido a esta dificuldade formas linearizadas são utilizadas.

Várias abordagens têm sido propostas para simplificar a expressão exata do coeficiente de reflexão de uma onda qP supondo uma onda qP incidente. Para meios fracamente anisotrópicos com alto grau de simetria e baixo contraste, os principais trabalhos foram de Thomsen (1986, 1993) e Banik (1987). Uma aproximação foi apresentada por Zillmer et al. (1997) considerando meios fracamente anisotrópicos e contrastes arbitrários. Entretanto, essa forma aproximada é ainda muito complexa. Pšenčik & Vavryčuk (1998) a particularizaram considerando pequenos contrastes entre as propriedades elásticas do meio obtendo uma fórmula mais simples tanto para o coeficiente de reflexão como para o coeficiente de transmissão de uma onda qP considerando uma onda qP incidente. Gomes (1999), Gomes et al. (2001) e mais recentemente Jílek (2001) apresentaram formas linearizadas para o coeficientes de reflexão de uma onda incidente qP e suas convertidas (R_{PP}, R_{SP} e R_{TP}) considerando ainda fraca anisotropia e fraco contraste. Neste trabalho é feita uma estimativa dos parâmetros elásticos a partir da inversão destas fórmulas linearizadas. É feito primeiramente uma análise de sensibilidade das formas linearizadas. Em seguida os parâmetros são estimados utilizando o inverso generalizado . Por fim são apresentados testes numéricos para um modelo onde o meio de incidência é um isotrópico e o meio subjacente é um meio TIV fracamente anisotrópico cujo eixo vertical de simetria foi girado e mergulhado. O ângulo de mergulho do eixo de simetria do modelo foi estimado.apartir da estimativa dos parâmetros elásticos

Análise de sensibilidade
Problemas lineares são representados matricialmente por:

$$\mathbf{y} = \mathbf{A}\,\mathbf{p}\,, \qquad (1)$$

em que: $\mathbf{y}$ é o vetor de observações, $\mathbf{p}$ é o vetor de parâmetros e $\mathbf{A}$ é a matriz sensibilidade determinada por $A_{ij} = \partial f_i / \partial p_j$ em que f_i é a i-ésima componente do funcional geofísico e p_j é a j-ésima componente do vetor de parâmetros. Neste trabalho o funcional geofísico é determinado pelas fórmulas linearizadas dos coeficientes R_{PP}, R_{SP} e R_{TP}.

Os parâmetros estimados estão relacionadas com os parâmetros reais por:

$$\mathbf{P}_{\mathbf{est}} = \mathbf{P}_{\mathbf{real}}\,\mathbf{R}\,, \qquad (2)$$

em que $\mathbf{R}$ é a matriz de resolução da matriz de sensibilidade (Tarantola, 1987). Verifica-se de (2) que quanto mais próximo da unidade estiver a diagonal principal da matriz de resolução melhor resolução terá os parâmetros estimados. Assim a estimativa dos parâmetros elásticos é analizada através da matriz de resolução de $\mathbf{A}$.

Foram testadas várias geometrias onde os ângulos de incidência e azimutais variavam. Essas geometrias são conhecidas no levantamento sísmico como walkway multiazimutal (Leaney, 1999). Verificou-se que a melhor estimativa dos parâmetros era encontrada quando a matriz de sensibilidade é formada pelas três fórmulas lineares juntas. Assim esta matriz de sensibilidade apresenta 21 colunas que correspondem os parâmetros e combinações dos parâmetros elásticos que caracterizam o meio. A forma com os parâmetros foram organizados é mostrada abaixo.

$P_1 = c_{11}$ $P_2 = c_{12} + 2c_{66}$ $P_3 = c_{13} + 2c_{55}$
$P_4 = c_{22}$ $P_5 = c_{23} + 2c_{44}$ $P_6 = c_{33}$
$P_7 = c_{44}$ $P_8 = c_{55}$ $P_9 = c_{14}$
$P_{10} = c_{15}$ $P_{11} = c_{16}$ $P_{12} = c_{24}$
$P_{13} = c_{25}$ $P_{14} = c_{26}$ $P_{15} = c_{34}$
$P_{16} = c_{35}$ $P_{17} = c_{36}$ $P_{18} = c_{45}$
$P_{19} = c_{46}$ $P_{20} = c_{56}$ $P_{21} = \rho$

A Figura 1 mostra a resolução dos 21 parâmetros elásticos para incidências de até 15^0 e para azimutes que variam de 30^0 em 30^0. De acordo com esta figura P_3 e P_5 apresentam pouca resolução. Os parâmetros apresentam resolução total para ângulos de incidência maiores. Entretanto, na prospecção sísmica os ângulos de incidência medidos são subnormais (ângulos próximos a normal), desta forma a geometria utilizada para gerar a matriz de resolução na figura acima apresenta a maior variação para o ângulo de incidência aceitável em sísmica.

Formulação do problema Inverso

A estimativa dos parâmetros elásticos foi feita utilizando-se à análise de SVD (Tarantola, 1987) a partir das fórmulas linearizadas. Utilizou-se o mesmo critério de corte adotado na análise de sensibilidade. Assim os parâmetros estimados são determinados por:

$$\mathbf{P}_{est} = \mathbf{V}\,\mathbf{S}^{-1}\,\mathbf{U}^T\,\mathbf{y}\,, \qquad (3)$$

em que $\mathbf{V}$ e $\mathbf{U}^T$ são matrizes cujas colunas são autovetores de $\mathbf{A}^T\mathbf{A}$ e $\mathbf{A}\,\mathbf{A}^T$ respectivamente e $\mathbf{S}^{-1}$ é a inversa da matriz diagonal dos valores singulares de $\mathbf{A}$.

A forma linearizada do coeficiente de reflexão de uma onda qP e suas convertidas são feita em torno de um meio de referência isotrópico e geral este meio é considerado como sendo a média da parte isotrópica dos meios de incidência e subjacente (Gomes et all, 2001). Para o problema da inversão o meio de referência isotrópico foi tomado de tal forma que a parte isotrópica nos dois meios foi considerada com sendo a mesma

Para meios TIVrotacionados, tem-se que o ângulo de mergulho do eixo de simetria pode ser determinado a partir dos parâmetros elásticos pelas fórmulas:

$$\tan 2\theta = \frac{2(c_{14} + 2c_{56} + c_{14} + c_{34})}{(c_{13} + 2c_{55} + c_{33}) - (c_{22} + 2c_{66} + c_{22})} \qquad (4)$$

A seguir é apresentado um exemplo numérico em que o ângulo de mergulho é estimado.

Teste numérico

A estimativa dos parâmetros elásticos é mostrada para um modelo onde o meio de incidência é um isotrópico cuja densidade, velocidade da onda P e velocidade da onda S são dadas respectivamente por $\rho = 2.65\,g/cm^3$, $\alpha = 4.20\,km/s$ e $\beta = 2.81\,km/s$. O meio em subjacente é um arenito TIV fracamente anisotrópico ($\delta = 0.09$) de acordo com os parâmetros de anisotropia de Thomsen, 1996. A densidade deste meio é de $\rho = 2.5 g/cm^3$ e o tensor elástico é dado por :

$$C_{\alpha\beta} = \begin{bmatrix} 59.80 & 16.17 & 14.75 & 0.00 & 0.00 & 0.00 \\ & 59.80 & 14.75 & 0.00 & 0.00 & 0.00 \\ & & 50.09 & 0.00 & 0.00 & 0.00 \\ & & & 19.80 & 0.00 & 0.00 \\ & & & & 19.80 & 0.00 \\ & & & & & 21.82 \end{bmatrix}. \qquad (5)$$

O meio foi girado de 60^0 em relação ao eixo z e mergulhado de 30^0.com relação ao eixo x.

As observações foram geradas de forma exata de acordo com as equações de Zoeppritz generalizadas (Gomes, 1999) e contaminadas com ruído gaussiano de 5% do maior valor das observações. Para a mesma geometria apresentada na Figura 1.

As Figura 2, 3 e 4 mostram os estereogramas dos coeficientes exatos de R_{PP}, R_{SP} e R_{TP}. Os coeficientes obtidos após a estimativa dos parâmetros elásticos apresentam ajuste de 0.0062 em relação aos coeficientes exatos. A tabela 1 abaixo mostra o contraste médio normalizado dos parâmetros elásticos exatos e dos parâmetros obtido após a inversão em torno do meio de referência.

Tabela 1- Parâmetros exatos, parâmetros estimados e o erro absoluto.

Parametro	Δ Par_exat	Δ Par_est	Erro
1	0.1507	0.1760	-0.0251
2	0.1583	0.1710	-0.0131
3	0.1220	-0.0620	0.1844
4	0.1650	0.1960	-0.0311
5	0.1260	-0.0370	0.1633
6	0.0900	0.0350	0.0545
7	0.0050	-0.0420	0.0476
8	0.0040	-0.0470	0.0514
9	0.0030	0.0420	-0.0394
10	-0.0216	0.1400	-0.1580
11	0.0062	-0.0280	0.0346
12	0.0130	-0.0480	0.0608
13	-0.0050	0.0380	-0.0437
14	0.0064	0.0003	0.0061
15	0.0110	0.0088	0.0021
16	-0.0020	-0.0151	-0.0037
17	0.0006	-0.0120	0.0126
18	0.0013	-0.0030	0,0044
19	-0.0080	0.0707	-0.0788
20	0.0042	0.0175	-0.0132
21	-0.0290	-0.0095	-0.0196

De acordo alguns parâmetros que na análise de sensibilidade apresentavam resolução total não apresentam boas estimativas após a inversão. Isto se deve ao fato de que as observações utilizadas na inversão do problema lineares foram geradas de forma exata e, portanto, os parâmetros estimados perderam resolução, uma vez que se está resolvendo um problema não linear de forma linear.

A seguir estimou-se o mergulho do eixo de simetria deste modelo através de (4). A estimativa para o ângulo de mergulho foi de 29.008^0 . Uma vez que o ângulo de mergulho exato é de 30^0, tem-se que a inversão apresenta resultados satisfatórios.

O ângulo de mergulho foi estimado em outros modelos com contraste dos parâmetros elásticos e anisotropia variáveis. A estimativa deste ângulo ficou em uma faixa de erro menor ou igual a 10^0 do valor real para modelos com contraste e anisotropia fracos ou moderados.

Outros fatores de influenciaram na estimativa dos parâmetros foi analisados, como a abertura do ângulo de incidência, influência do fator k, sensibilidade ao meio de referência.

Abertura do ângulo de incidência

Foram feitos testes considerando aberturas angulares de 20^0, 25^0 e 30^0. Ainda que a análise de sensibilidade mostre que os parâmetros elásticos ganham resolução com maior incidência, verificou-se que quanto maior o ângulo de incidência pior ficava as estimativas dos parâmetros elásticos. Isto se deve a fato de que as fórmulas linearizadas só possuem validade a para incidências subnormais, o que está de acordo com a prospecção sísmica.

Influência do fator k

O fator k corresponde à razão entre a média da velocidade da onda cisalhante e a média da velocidade da onda longitudinal em relação aos dois meios. Foram feitos testes considerando k variando de 10% e 50% do valor real de k. Os resultados mostram que as estimativas são sensíveis ao valor de k. Nestes testes para um mesmo modelo, a estimativa do mergulho oscila em uma faixa de 10^0 aproximadamente do valor real do mergulho.

Sensibilidade ao meio de referência

Neste trabalho o meio de referência foi escolhido de forma arbitrária. De acordo com os testes verificou-se que dependendo da escolha deste meio de referência os contrastes de impedância podem tornar-se consideráveis tendo-se, portanto, um domínio onde as linearizações não são mais válidas. O meio de referência deve então ser escolhida de tal forma que o pressuposto de fraco contraste deva ser respeitado.

Outro fator de grande importância verificado nos testes realizados é que as estimativas são mais sensíveis ao pressuposto de fraco contraste que fraca anisotropia.

Conclusão

A análise do problema de inversão de coeficientes de reflexão utilizando aproximações lineares para a refletividade de ondas qP foi efetuada através da decomposição em valores singulares. A inversão linearizada apresenta resultados satisfatorios na recuperação do constraste de densidade e de constantes elástica para modelos com fraca anisotropia e fraco contraste de impedância. Dentre deste limites é possível estimar a orientação do eixo de simetria de um meio TI e portanto a orientação de fraturas utilizando dados de toda a refletividade qP. Estes resultados não se mantem principalmente quando aumenta o constraste de impedância. Para meios com maior contraste de propriedades elasticas e maior anisotropia a inversão não linear destes coeficientes torna-se necessária para que se possa estimar com melhor precisão os parâmetros elásticos do meio em subsuperfície.

Referencias

Banik**,** N**.** C**.,** 1987. An effective anisotropy parameter in transversely isotropic media. Geophysics, 52: 1654-1664.

Gomes, E.,1999. Reflectivity of P waves in anisotropic media (in portuguese). Tese de Mestrado. Departamento de Matemática da Universidade Federal do Pará, Brasil.

Gomes, E., Protazio, J.S, Costa, J. Simões-Filho, I.A.,2001. Linearization of qP wave reflection coefficients in anisotropic media(in portuguese). Accepted for publication in Brazilian Journal of Geophysics.

Jílek, P. , 2001, Converted PS-wave reflection coefficients in weakly anisotropic media. Accepted for publication in Pure and Applied GeophysicsLeaney, W. S., Sayers, C. M. and Miller, D. E., 1999. Analysis of multiazimuthal VSP data for anisitropy and AVO: Geophysics, 64, 4, 1172-1180.

Leaney,W.S, Sayers, C. M. and Miller,D.E., 1999, Analysis of multiazimuthal VSP data for anisotropy and AVO: Geophysics, 64, n^0 4, 1172-1180

Tarantola, A.,1987. Inverse problem thetory. Methods

for data fitting and model parameter estimation. Elsevier, Amsterdam.

Vavryčuk, V. & Pšenčik, V.,1998. PP-Wave reflection coefients in weakly anisotropic elastic media. Geophysics,vol 63,6,2129-2141.

Thomsen, L.,1986. Weak elastic anisotropy. Geophysics,vol 51,10,1954-1966.

Thomsen 1993. Weak elastic anisotropic reflection. In Castagna, J. P. and Backus, M. M. Eds. Offset-dependent reflectivity-Theory and practice AVO analysis: Soc. Exp. Geophys. 103-111.

Zillmer, M., Gajewski, D. & Kashtan, B. M., 1997, Reflection coefficients for weak anisotropic. Geophys. J. Internat, 129, 389-398.

Agradecimentos

Os autores agradecem o suporte finaceiro do projeto FINEP/CNPq/Pronex em Engenharia de reservatórios.

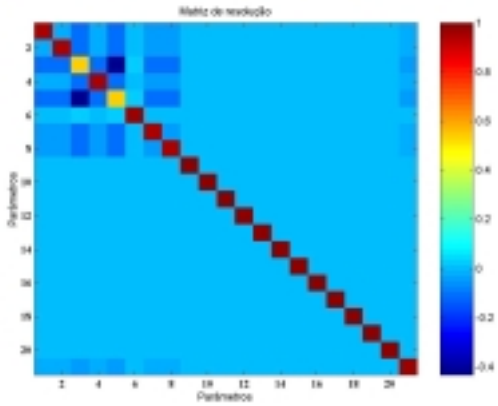

Figura 1- Matriz de resolução obtida das fórmulas linearizadas dos coeficientes de reflexão, para um posto efetivo de **A** o valor absoluto 0.01.Verifica-se que há dependência linear entre os parâmetros físicos.

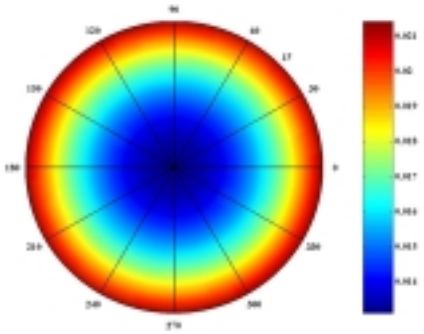

Figura 2 – Estereograma com o coeficiente de reflexão R_{PP} exato. O azimute varia de 0^0 até 360^0 e está representado pelos raios na figura. A incidência varia de 0^0 até 15^0 a partir da normal à interface que separa os planos.

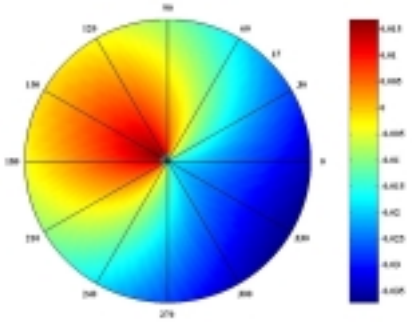

Figura 3 – Estereograma do coeficiente de reflexão R_{SP} exato.

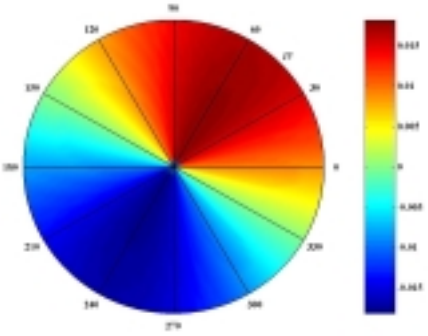

Figura 4 – Estereograma do coeficiente de reflexão R_{TP} exato.

Local inversion for anisotropy from qP-wave slowness and polarization vectors

Ivan Pšenčík, Xuyao Zheng*, Steve Horne** and Scott Leaney***

*) *Academy of Sciences, Boční II, Praha 4, Czech Republic, e-mail: ip@ig.cas.cz, zheng@ig.cas.cz*

**) *Schlumberger, Buckingham Gate, Gatwick, RH6 0NZ, UK, e-mail: shorne@slb.com, leaney@slb.com*

Abstract

Data from multi-azimuthal walkaway VSPs are very useful for detection and determination of local anisotropy at individual receivers in a borehole. Various inversion techniques have been proposed. They differ by assumptions about properties of the medium surrounding receivers, by types of waves involved and by computational methods used for the inversion. We present a technique based on the first-order perturbation theory for anisotropic media. Basic equations of our technique are applicable to the data of qP waves propagating in laterally inhomogeneous, weakly anisotropic media of arbitrary symmetry. The data are components of polarization and slowness vectors of qP waves generated at surface sources and recorded at a given receiver. For each source, we thus have an equation. The SVD algorithm is used to solve an overdetermined system of equations for weak anisotropy (WA) parameters. From them qP-wave phase velocity can be reconstructed. We test the technique on a set of synthetic multi-azimuthal walkaway VSP data and on a set of walkaway VSP data measured in the Java Sea region. In the former case, true anisotropy of the model is known, in the latter case, the results of inversion can be compared with results of other techniques. In both cases good agreement is found.

Introduction

Let us consider a multi-azimuthal multiple-source offset VSP experiment with three-component downhole recordings unaffected by a free surface. Attempts to determine anisotropy parameters from data measured in such an experiment are not new. It is quite common to derive slowness components from such data and use them for the determination of anisotropy (White et al., 1983; Gaiser, 1990). If only a component of the slowness vector is available, the use of polarization information becomes a necessity, see Zheng and Pšenčík (2001). In most attempts, VTI anisotropy (transverse isotropy with vertical axis of symmetry) has been assumed (Hsu et al., 1991; de Parscau, 1991; Williamson et al., 2000). Horne et al. (1998) and Horne and Leaney (2000) proposed a method based on the simultaneous use of components of slowness and polarization vectors, which can be used in media with arbitrary structural complexities in the overburden, and can be applied, in principle, to anisotropy of arbitrary symmetry. Their method minimizes the difference between observed and calculated components of slowness vectors corresponding to the observed polarization directions. Forward modelling uses a numerical search for the slowness direction corresponding to the observed polarization. Adaptive simulated annealing is used to minimize the objective function. Horne and Leaney (2000) apply the method to qP and qS direct and reflected waves.

The algorithm used in this paper represents an alternative to the above approach. It is based on the first-order perturbation theory for anisotropic media, see Jech and Pšenčík (1989). Zheng and Pšenčík (2001) have shown that the perturbation formulae relating slowness and polarization vectors of a qP wave to 15 weak anisotropy (WA) parameters describing this wave (Pšenčík and Gajewski, 1998) can be transformed into a single linear equation if only the component of the slowness vector along the borehole is known (this is the case in most applications). This equation corresponds to a single source-receiver pair. Multi-azimuthal walkaway experiments thus produce large systems of such equations, which can be solved for WA parameters at a receiver. The medium in which a receiver is situated can be laterally inhomogeneous (no requirement of local homogeneity is necessary) and anisotropy of arbitrary symmetry can be dealt with. The only assumption is that the anisotropy is weak. Thanks to the use of the perturbation theory the equations have a very simple and transparent form. Since weak anisotropy is common for many real materials (Thomsen, 1986), the equations have a broad applicability.

The algorithm proceeds as follows. For the estimation of components of slowness and polarization vectors various approaches can be used. One way is the parametric inversion approach proposed by Esmersoy (1990) for two downgoing wavefields and extended to N wavefields by Leaney (1990). Given slowness and polarization data we find the isotropic reference medium from which we seek the weakly anisotropic medium and construct rays in this medium connecting sources and the receiver. Information about these rays and about compo-

nents of slowness and polarization vectors is used for the formation of an overdetermined system of linear equations at each receiver, from which the WA parameters can be determined.

Formulae

For the determination of WA parameters we use Eq.(22) of Zheng and Pšenčík (2001):

$$(\alpha^2-\beta^2)^{-1}(B_{13}X^{(2)}-B_{23}X^{(1)})-\frac{1}{2}\alpha^{-2}B_{33}\eta = (X^{(2)}e_i^{(1)}-X^{(1)}e_i^{(2)})g_i+\alpha\Delta\eta(X^{(1)}e_3^{(2)}-X^{(2)}e_3^{(1)}+\alpha\eta^2). \quad (1)$$

The symbols α and β are the P- and S-wave velocities of the reference medium, the symbols g_i the polarization vectors. The vectors $e_i^{(1)}$, $e_i^{(2)}$ are two mutually perpendicular unit vectors, perpendicular to the vector $e_i^{(3)}$, the phase normal of the P wave in the reference isotropic medium. The symbols B_{mn} denote elements of the *weak anisotropy* matrix,

$$B_{mn}=\Delta a_{ijkl}e_i^{(m)}e_j^{(3)}e_l^{(3)}e_k^{(n)}, \quad (2)$$

in which Δa_{ijkl} is the deviation of elastic parameters of the anisotropic medium from elastic parameters of the isotropic reference medium. The elements B_{13}, B_{23} and B_{33} can be expressed in terms of 15 WA parameters, see Zheng and Pšenčík (2001). The WA parameters are the sought unknowns in Eq.(1). The symbols $X^{(K)}$, $(K=1,2)$ are defined as

$$X^{(K)}=\xi e_2^{(K)}-\zeta e_1^{(K)}. \quad (3)$$

The symbols ξ, ζ and η denote sizes of radial, transverse and vertical components of the slowness vector in the reference medium, $\Delta\eta$ is the deviation of the vertical component of the observed slowness vector from the reference medium.

Synthetic test

For this test we use the VSP configuration shown schematically in Fig. 1. The model is confined in a model box whose horizontal dimensions are 10 × 10 km. The borehole is situated in the center of the box. The model is laterally inhomogeneous and of TI symmetry. The qP-wave anisotropy is about 8%. The elastic parameters are chosen so that the symmetry axis at the horizontal top surface (the depth of 0 km) is inclined by 10^o from horizontal and rotated by 25^o from the x-axis. The axis of symmetry at the bottom surface is horizontal and parallel with the x-axis. The bottom surface is an inclined plane. Between the top and the bottom surfaces the elastic parameters are determined by linear interpolation. The inclined bottom surface of the TI model introduces lateral inhomogeneity into the model.

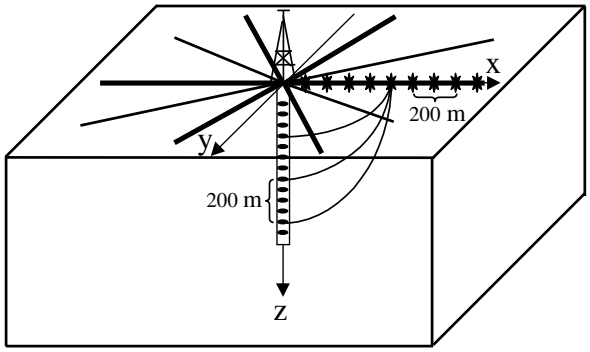

Figure 1: Multi-azimuthal multiple-source offset VSP experiment configuration: 5 radial surface profiles (the 3-profile experiment by thick lines) with 9 shots to each side of the borehole, with 0.1 km separation; 13 three-component receivers in the borehole with 0.05 km separation.

We consider 3 or 5 surface profiles with their center at the mouth of the borehole, see Fig. 1. The 3 profiles are distributed uniformly with the step of 60^o (0^o, 60^o and 120^o), measured from the positive x-axis. The 5 profiles are associated with angles 0^o, 30^o, 60^o, 120^o and 150^o. Each profile contains 9 sources at each side of the borehole, starting at 0.1 km from the mouth of the borehole and separated by 0.1 km. The vertical borehole contains 13 three-component receivers starting at a depth of 0.1 km and separated by 0.05 km. The free surface effects are neglected throughout the experiment. For the 3 profile experiment 54 equations (1) are constructed to solve for the 15 WA parameters. For the 5 profile experiment there are 90 equations.

"Observed" synthetic seismograms were generated using the program package ANRAY (Gajewski and Pšenčík, 1990). From the seismograms, arrival times were picked and particle motion diagrams were constructed. Picked travel times from five neighbouring receivers were used to determine the best fitting hyperbola, from which the partial derivative of the travel time with respect to the $z-$coordinate was found. Polarization vectors, g_i, are computed from least square fits to the observed particle motions of the first arrivals.

The observed travel times were used to determine an approximate 1-D distribution of the P-wave velocity α. The S-wave velocity β was taken as $\beta=\alpha/\sqrt{3}$. Then the rays from the source

to individual receivers were traced in the reference medium. Normalized slowness vectors at receivers yielded the phase normal $e_i^{(3)}$, with respect to which, the vectors $e_i^{(1)}$ and $e_i^{(2)}$ were defined.

For solving the resulting system of equations (1), the SVD method was used. In Fig. 2, equal area plots of isolines of the qP-wave phase velocity obtained from inversion (thin lines) and from the true model (thick lines) are compared. Solid circles denote a longitudinal direction which coincides with the symmetry axis in the true model. The open circles indicate longitudinal direction obtained from inversion. The left column in Fig. 2 shows results for 3 profiles, the right column for 5 profiles. In each column, results for the receivers 4, 7 and 10 situated at depths z=0.25, 0.4 and 0.55 km are shown.

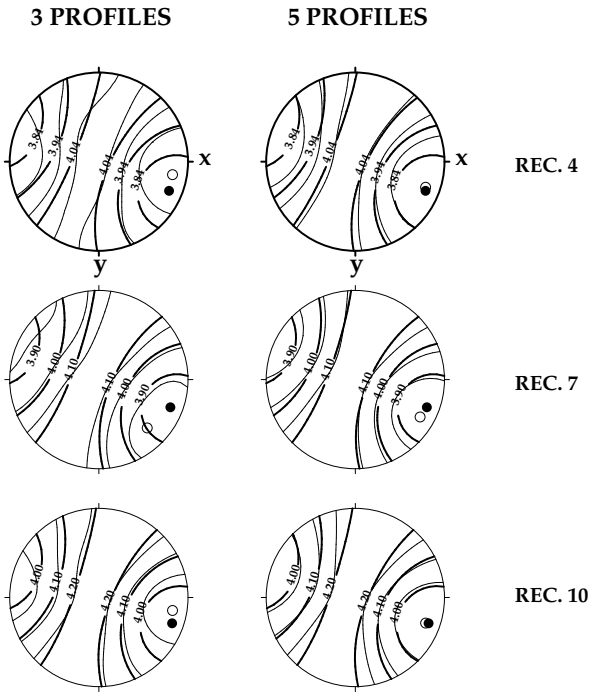

Figure 2: Equal area plots of phase velocity obtained from inversion (thin lines) and for the true model (thick lines). Solid and open circles denote the true and inverted longitudinal directions.

We can see that the thin curves in Fig. 2 have a more complicated form than the thick curves, which correspond to the TI model. This means that the inverted model no longer possesses TI symmetry. As expected, the fit between true and inverted phase velocities is better for 5 profiles. The best overall fit is observed for receiver 4. Isolines of the true and inverted model fit each other well not only in the centre of the circle, i.e., for vertical direction, but also at the border of the circle, i.e., for horizontal directions. This picture changes when moving to deeper receivers. For the receiver 10, a good fit can be observed at the centre of the circle. Towards the border of the circle the misfit increases. This indicates insufficient illumination of receivers with increasing depth. Longitudinal directions are obviously better determined for 5 profiles.

Field data

We apply the above inversion scheme to the walk-away VSP data of Horne and Leaney (2000). The main difference with the previous synthetic test is that we deal now with a single profile. We concentrate on direct and reflected qP waves only. The waves are generated by 228 sources distributed along a single profile on the Earth's surface. The sources extend from -2.5 to 2.5 km with, approximately, 25m spacing. We have at our disposal only vertical components of slowness and polarization vectors. No assumptions are made about the remaining components of the slowness vector. The polarization vector is assumed to be confined to the vertical plane containing the profile and the borehole. Because we have available data from a single profile only, we can recover only 5 of 15 WA parameters. For 228 sources, we have a system of 228 equations if only downgoing qP wave is considered and 456 equations if both downgoing and upgoing qP waves are considered. We solve these equations for the above 5 WA parameters.

Fig. 3 shows a plot of scaled vertical component of the slowness vector versus the vertical component of the polarization vector g_z. The quantity g_z is maximum when the polarization vector is vertical. To the sides, g_z decreases. The left-hand side corresponds to the positive, the right-hand side to the negative branch of the profile. The vertical coordinate is specified by the quantity αp_z, which specifies approximately the vertical component n_z of the phase normal. The data and the thin curve in the upper frame correspond to downgoing waves only. The data and the thin curve in the lower frame correspond to upgoing waves only. Remaining curves are the same in both frames and show results of inversion considering all qP waves (thick curve) and results of Horne and Leaney (2000) for slowness (slow) and slowness plus polarization (slow+pol) inversion. The dotted curve corresponds to the reference isotropic medium. Although only qP-waves were used, results are similar to results of Horne and Leaney (2000), which were obtained after sampling 10000 models.

Comparison of vertical sections of phase velocity reconstructed from results of Horne and Leaney (2000) and from the solution of system of equations

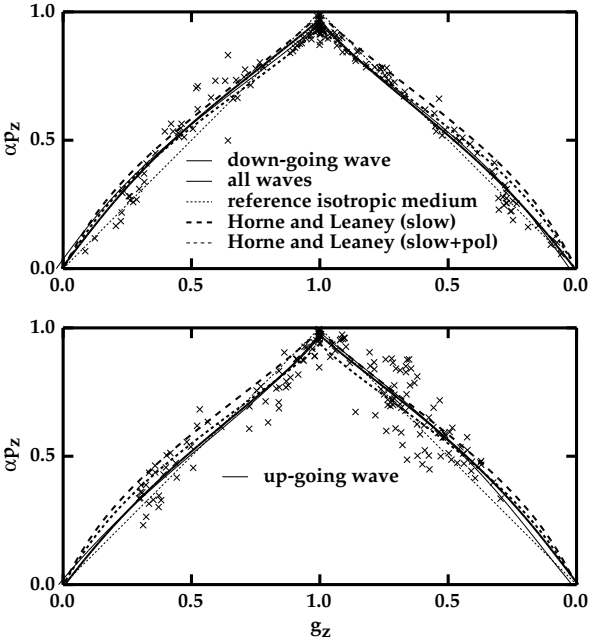

Figure 3: Scaled vertical components of slowness vector versus vertical component of the polarization vector. Crosses denote observed data.

(1) seems to indicate stronger anisotropy (about 14% and 19%) for the former inversion and only about 8% for the latter one, which also seems to indicate an inclined axis of symmetry. We are now analyzing if the differences are significant and if yes, whether they are caused by neglecting qS waves.

Conclusions

Techniques based on the first-order perturbation theory can be used for inversion of components of slowness and polarization vectors from multi-azimuthal or single profile walkaway VSPs for WA parameters. Consequently, the WA parameters can be used for the approximate construction of a phase velocity surface. Tests on synthetic and field data seem to indicate that the technique, although approximate, may yield good quality results.

In these tests, we assumed that the studied medium is generally anisotropic. If there are indications of higher symmetry, it is easy to specify the technique for such a higher symmetry anisotropy, see Zheng and Pšenčík (2001). Generalization for qS waves is under preparation.

References

de Parscau, J., 1991, P- and SV-wave transversely isotropic phase velocities analysis from VSP data: Geophys. J. Int., **107**, 629–638.

Esmersoy, C., 1990, Inversion of P and SV waves from multicomponent offset vertical seismic profiles: Geophysics, **55**, 39–50.

Gaiser, J. E., 1990, Transversely isotropic phase velocity analysis from slowness estimates: J. Geophys. Res., **95**, 11241–11254.

Gajewski, D., and Pšenčík, I., 1990, Vertical seismic profile synthetics by dynamic ray tracing in laterally varying layered anisotropic structures: J. Geophys. Res., **95**, 11301–11315.

Horne, S., and Leaney, S., 2000, Polarization and slowness component inversion for TI anisotropy: Geophysical Prospecting, **48**, 779–788.

Horne, S., McGarrity, J., Sayers, C., Smith, R. and Wijnands, F., 1998, Fractured reservoir characterisation using multi-azimuthal walkaway VSPs: Expanded Abstracts, 68th Ann. Internat. Mtg., SEG, 1640–1643.

Hsu, K., Schoenberg, M. and Walsh, J., 1991, Anisotropy from polarization and moveout: Expanded Abstracts, 61st Ann. Internat. Mtg., SEG , 1526–1529.

Jech, J., and Pšenčík, I., 1989, First-order perturbation method for anisotropic media: Geophys. J. Int., **99**, 369–376.

Leaney, S., 1990, Parametric wavefield decomposition and applications: Expanded Abstracts, 60th Ann. Internat. Mtg., SEG, **99**, 1097-1100.

Pšenčík, I., and Gajewski, D., 1998, Polarization, phase velocity and NMO velocity of qP waves in arbitrary weakly anisotropic media: Geophysics, **63**, 1754–1766.

Thomsen, L., 1986, Weak elastic anisotropy: Geophysics, **51**, 1954–1966.

White, J. E., Martineau-Nicoletis, L. and Monash, C., 1983, Measured anisotropy in Pierre shale: Geophysical Prospecting, **31**, 709–725.

Williamson, P., Maocec. E. and Boelle, J-L., 2000, Local estimation of anisotropy parameters from well seismic polarisation data: Expanded Abstracts, 70th Ann. Internat. Mtg., SEG, 2241–2244.

Zheng, X., and Pšenčík, I., 2001, Local determination of weak anisotropy parameters from qP-wave slowness and particle motion measurements: PAGEOPH, accepted for publication.

Phase Correction in Separating P- and S-Waves in Elastic data

Robert Sun, Department of Earth Sciences, National Chengkung University, 1 Tahsueh Rd., Tainan, Taiwan 701.*
E-mail: sun@geotech.et.ncku.edu.tw

Summary

The P- and S-waves separated from elastic data have wavelets that are phase shifted π/2 compared to the wavelets of the input elastic data. This phase shift is a direct result of the spatial derivatives in computing dilatation (divergence, representing P-waves) and rotation (curl, representing S-waves). It is unwanted and can be corrected by imposing a –π/2 phase shift, using Hilbert transform with respect to time, on the separated P- and S-waves.

Introduction

Sun (1999) developed an algorithm to separate P- and S-waves in two-dimensional elastic data. The algorithm includes: (1) downward extrapolating the elastic data in an elastic velocity model using elastic wave equation; (2) computing the dilatation to represent pure P-waves and computing the rotation to represent pure S-waves at some depth; (3) upward extrapolating the dilatation in a P-velocity model and upward extrapolating the rotation in an S-velocity model, using acoustic wave equation. The parameters in elastic data are displacement components. Computing dilatation and rotation involves spatial derivatives on displacement components that induce a π/2 phase shift. A π/2 phase shift makes the wavelet complicated and is unwanted.

This paper intends to correct the π/2 phase shift. Although this phase shift is induced in the derivatives with respect to spatial variables, correction is performed in time domain because of easiness.

Theory

Let $\mathbf{U_P}$ denote the displacement vector of the propagating P-wave. Lame's theorem (Aki and Richards, 1980) stated that $\mathbf{U_P}$ can be derived as the gradient of a scalar compressional potential A:

$$\mathbf{U_P} = \nabla \mathrm{A} . \qquad (1)$$

For a harmonic plane wave, the compressional potential A can be expressed as a scalar function

$$\mathbf{A} = -ie^{i\left(k_{px}x+k_{pz}z-wt\right)}, \qquad (2)$$

where k_{px} and k_{pz} are the P-wave spatial wavenumbers in x- and z-direction, respectively, w is the angular frequency, t is time, and $i = \sqrt{-1}$. Then the displacement vector $\mathbf{U_P}$ can be derived by substituting (2) into (1), and the result is

$$\mathbf{U_P} = \left(k_{px}\boldsymbol{a}_x + k_{pz}\boldsymbol{a}_z\right)\ e^{i\left(\boldsymbol{k}_{px}x+k_{pz}z-wt\right)}, \qquad (3)$$

where $\boldsymbol{a}_x$ and $\boldsymbol{a}_z$ are the unit vectors in the x- and z-directions, respectively.

At separating P- and S- waves, the dilatation ϕ is computed as the divergence of $\mathbf{U_P}$ to represent the P-waves:

$$\phi(x,z,t) = \nabla\cdot\mathbf{U_P} = i\left(k_{px}^2 + k_{pz}^2\right)\ e^{i\left(k_{px}x+k_{pz}z-wt\right)}. \qquad (4)$$

The divergence of the S-wave displacement does not appears in (4) because it is zero. (3) and (4) show that the dilatation ϕ differs from the P-wave displacement $\mathbf{U_P}$ in, among others, that the harmonic term $\exp[i(k_{px}x + k_{pv}y - wt)]$ in (4) is multiplied by a factor i, whereas that in (2) is not. The factor i, which is $\exp(i\pi/2)$, causes a π/2 phase shift and is the origin of the phase shift in the separated P-waves. Similarly reasoning will illustrate that a π/2 phase shift appears in the separated S-waves.

The π/2 phase shift on ϕ can be corrected by imposing a –π/2 phase shift. Since the factor i in (4) is multiplied to the entire harmonic term $\exp[i(k_x x + k_y y - wt)]$ rather than to the spatial variables x or z, we have the freedom to perform the –π/2 phase shift in t domain rather than in x-z domain. Since (4) can be rewritten as

$$\phi(x,z,t) = \phi_0\left(k_{sx}^2 + k_{sz}^2\right)\ e^{i\left(k_{sx}x+k_{sz}z\right)}\left(ie^{-iwt}\right), \qquad (5)$$

the factor i in (4) can be removed by Hilbert transform with respect to t.

The π/2 phase shift in the separated S-waves can be treated similarly.

A synthetic example

Figure 1 shows an isotropic, two-dimensional laterally inhomogeneous elastic model of 4.0 km horizontal extent and 2.2 km depth extent, with one dipping reflector and one horizontal reflector. The synthetic common-source elastic data generated for this model with source at (x,z) = (2.0 km, 0.14 km) is presented in Figure 2. Only the reflected waves are included in Figure 2. The P-waves (Figure 3a) and S-waves (Figure 3b) extracted at depth z_1 = 0.2 km are obviously phase shifted π/2.

Hilbert transform is performed on each trace in Figures 3a and 3b to obtain the resulting phase-corrected P- and S-

waves at depth z_1. Then they are upward extrapolated using acoustic wave equation. The P- and S-waves extracted at the earth's surface are in Figures 4a and 4b. They have been phase corrected since the wavelets in them are the same as those in the input elastic data (Figure 2).

Conclusions

The algorithm to separate P- and S-waves enables a person to handle elastic data by pure P- and S-waves independently. Yet the presence of the unwanted $\pi/2$ phase shift in the wavelets is unavoidable. This paper shows that the phase of the wavelets can be corrected by applying Hilbert transform with respect to t after the P- and S-waves have been separated.

The $\pi/2$ phase shift is induced in the derivatives with respect to x and z. But it is uneasy to correct the phase in x-z domain. Performing Hilbert transform with respect to t is easy and effective.

Reference

Aki, K., and Richard, P. G., 1980, Quantitative Seismology: Freeman Co.

Sun, R., 1999, Separating P- and S-waves in a prestack 2-dimensional elastic seismogram: Geophysics, submitted.

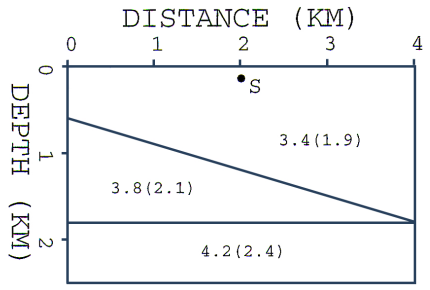

FIG. 1. A laterally inhomogeneous elastic model from which the synthetic elastic seismogram is generated. The numbers outside the parentheses denote P-velocities, and the numbers in the parentheses denote S-velocities (in km/s). S = source location.

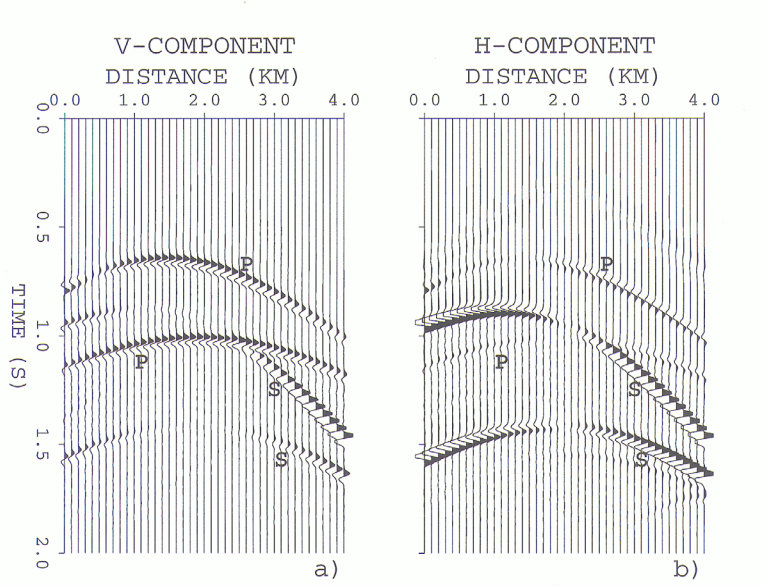

FIG. 2. Synthetic common-source elastic data generated from the model in Figure 1. (a) Vertical component; (b) horizontal component. P = P-wave; S = S-wave.

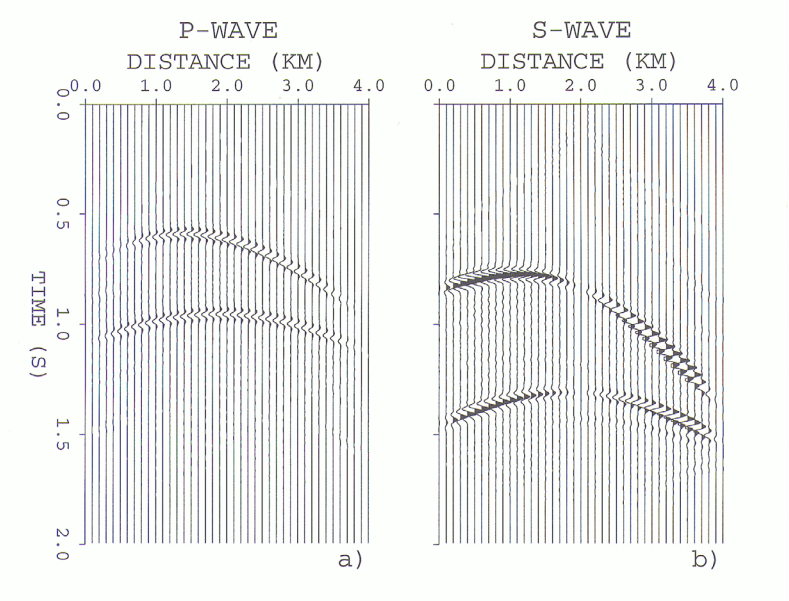

FIG. 3. Separated (a) P-waves and (b) S-waves extracted at depth 0.2 km.

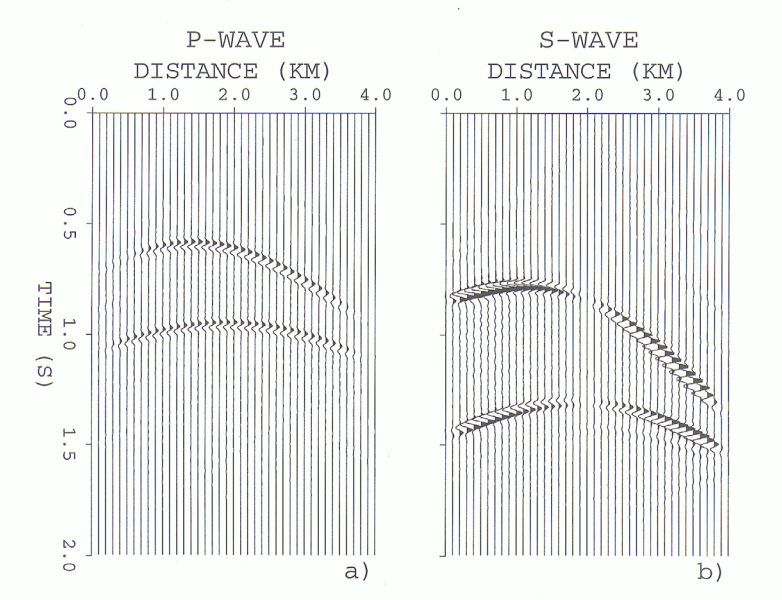

FIG. 4. The separated and phase corrected (a) P-waves and (b) S-waves extracted at the earth's surface.

Processing and Analysis of PS-wave Data from a 3-D/3-C Land Survey for Fracture Characterization

James Gaiser, Richard Van Dok, and John Markert, WesternGeco, Denver

Abstract

The investigation of S-wave birefringence (splitting) using 3-D converted P to S-waves (PS-waves) is an important tool for characterizing reservoir fractures. In azimuthally anisotropic media, fracture intensities are directly related to traveltime differences between the fast and slow S-waves and fracture orientations are related to the polarization direction of the fast S-wave. These effects are accurately analyzed in a 3-D/3-C survey from the Green River basin in Wyoming to preserve meaningful azimuthal variation in amplitude and traveltime. Estimates of the principal PS-wave fast and slow directions (PS_1 and PS_2) are made early in the processing to guide propagation azimuth limitations during processing. In preparation for advanced fracture analysis techniques, the data are processed in common-azimuth volumes and all azimuths are combined using 2Cx2C Alford rotation into a single group after azimuthal residual statics. Ratios of PS_1 and PS_2 average vertical velocity are particularly important to identify the vertical extent of overburden anisotropy, as well as reservoir horizons. Overburden effects can be removed by 2Cx2C rotation and layer-stripping analyses before characterizing deeper horizons. In addition, less quantitative attributes such as residual off-diagonal 2Cx2C amplitudes and isochron differences between PS_1 and PS_2 are shown.

Introduction

Recent interest in the use of PS-waves to help characterize fractured reservoirs has prompted the acquisition of several multicomponent surveys around the industry. Ata and Michelena (1995) used three 2-D lines centered over a well to quantify fracture information. Although the spatial coverage was sparse, azimuthal anisotropy appeared to be caused by two fracture systems. A small 3-D/3-C survey collected in the Wind River basin in Wyoming to calibrate a larger P-wave effort had some measure of success in characterizing fracture anisotropy (Gaiser, 1999; and Grimm et al., 1999). In 2000, the first marine 3-D/3-C survey was acquired at the Emilio field in the Adriatic for the purpose of characterizing fracture porosity (Gaiser et al., 2001).

The objective of this study was to use a PS-wave seismic survey in the Green River basin in Wyoming to quantitatively identify fractured areas in a naturally fractured Cretaceous sandstone reservoir at depths between 3,000 and 4,500 m. A 3-D/3-C survey was designed and acquired to provide wide azimuth and offset coverage at the target. The receiver lines were oriented E-W and a diagonal brick shot pattern was acquired to yield a CMP fold of approximately 24 over 50 km^2.

Data Processing

Initial processing of the horizontal data included rotation to the radial and transverse components in a source-centered coordinate system (Gaiser, 1999), geometric spreading corrections, surface-consistent deconvolution, and time-variant spectral whitening. Source statics computed from the P-wave processing were also applied to the PS-wave data, as well as elevation corrections at the receivers. Preliminary stacking velocities were estimated and an initial common-conversion point (CCP) binning correction was applied to the data. Five passes of residual receiver statics were computed while iterating with additional passes of velocity analysis and anisotropic, depth-dependent CCP binning.

At two key well locations, a large azimuth supergather measuring 536 by 670 m (17 x 21 CCP gathers) was extracted, consisting of radial and transverse component azimuthal stack traces every 10 degrees. The transverse component showed clear polarity reversals every 90 degrees and the radial component demonstrated a variation in traveltime with azimuth. The fast PS_1 direction was approximately N135E and the slow PS_2 direction N225E at both well locations. The data volume was limited to the PS_1 and PS_2 propagation directions (+/-22.5°) stacked and migrated. Additional residual receiver-static corrections were computed using these limited azimuth volumes and improved stacks.

In preparation for subsequent fracture detection analysis, the entire data volume, both radial and transverse components, was divided into eight common-azimuth sectors; 0 to 360 deg, incrementing by 45 deg with a tolerance of +/-22.5 deg. The transverse component data was processed using the same deconvolution operators, statics, and velocities estimated from the radial component data. All volumes were migrated using the same migration velocity field. This resulted in 16 separate common-azimuth volumes of radial and transverse data. These components exhibited azimuthally varying traveltimes and to combine them into a single dataset for improved fold and enhanced signal, 2Cx2C Alford (1986) rotations, adapted for PS-waves (Gaiser, 1999), were applied. Each of the eight 2Cx2C sets was rotated into the

preferred fast (PS_{11}) and slow (PS_{22}) directions (N135E and N225E) and stacked to create one set of 2Cx2C data for further analysis. This increased the fold and resulted in improved signal quality.

However, small residual time shifts between PS_{11} and PS_{22} were observed in the data for each of the eight common-azimuth directions and components. To correct for this and improve the combined stack, azimuth-consistent static corrections were computed to align the radial component data in both the PS_{11} and PS_{22} propagation directions. After applying these corrections to the radial and respective transverse components for each azimuth direction the resulting stacks were significantly improved (Fig. 1).

Birefringence Analysis

One of the most important steps in using PS-waves for fracture detection is to quantify the overburden azimuthal anisotropic properties. These properties include the orientation of the principal S-wave directions, used to identify fast and slow waves for processing, and the differential velocity between the fast and slow waves. Another important property of the overburden is the vertical extent. One approach to estimate the S-wave azimuthal anisotropy in the overburden is to analyze PS_{11} and PS_{22} velocity ratios (Gaiser, 1996) as a function of two-way vertical time. Figure 2 shows an analysis between PS_{11} and PS_{22} data located at the well in the northern part of the survey. The vertical axis is PS_{11} two-way time and the horizontal axis is the ratio of Vps_{11}/Vps_{22} average velocity. Variable density represents positive cross-correlation coefficients between the two waves. Depending on the velocity ratio, PS_{22} is stretched (< 1.0) or compressed (> 1.0), and correlated with the PS_{11} at predefined window times. Contours superimposed on the plot indicate constant time delays of PS_{22} in milliseconds.

A maximum correlation trend can be clearly interpreted and is indicated by the dashed line. This corresponds to the time-variant velocity ratio of Vps_{11}/Vps_{22}. Above 1.0 s the trend is unknown. However, below 1.0 s the trend increases to a maximum at about 1.3 s and then roughly follows a 30 ms PS_{22} time delay. In the absence of the upper 1.0 s of data, the base of the overburden can be interpreted at about 1.5 s. It represents an interval of relatively homogeneous, azimuthally anisotropic material with constant orientation confirmed by azimuth-supergather analyses. Notice that the trend increases to the 40 ms PS_{22} time delay contour at about 3.0 s, indicating an increase in S-wave birefringence.

Further processing of the overburden involves 2Cx2C rotation and Winterstein and Meadows (1991) layer stripping to remove the azimuthal anisotropic effects imparted on the PS-wave data. This can be accomplished over a time window from 0.0 to 1.6 s. After layer stripping, the data are in position for further analysis to determine principal S-wave directions and percent anisotropy for deeper intervals. Figure 3 shows the 2Cx2C-inline section that intersects the well at the vertical white line. PS_{11} and PS_{22} are the principal components and are aligned down to the base of overburden at about 1.6 s. The off-diagonal components (PS_{12} and PS_{21}) have been minimized to this same event.

One approach to analyze target horizons below the overburden is to interpret residual amplitudes on the PS_{12} and PS_{21} components spatially and temporally. These amplitudes can result when there are changes in the S-wave birefringence principal directions. Such changes may be too subtle to be quantified by traditional layer-stripping methods or by velocity ratios, but amplitudes are sensitive to these variations in S-wave properties and can give qualitative insights into regions where fracturing may be more intense and change orientation.

A more quantitative approach is to measure traveltimes between reflections bracketing targets for both the PS_{11} and PS_{22} waves in the volume in Figure 3. By comparing isochron differences between PS_{11} and PS_{22}, a spatial representation of percent anisotropy can be interpreted for lateral variations in fracture intensity. The assumption here is that there is little or no change in the orientation of the principal axes, since rotations are not involved.

The third approach, which is most quantitative, involves layer stripping below the overburden. Off-diagonal components are minimized further by 2Cx2C rotations to estimate any change in the direction of the principal axes. After minimization, the separated PS_{11} and PS_{22} waves are correlated and PS_{22} is aligned with PS_{11}. These properties can be interpreted as lateral variations in fracture orientation and intensity.

Conclusions

Early estimation of the principal S-wave orientation is critical to optimize processing for fracture characterization. This can be accomplished using azimuth supergather analyses at selected locations and limiting propagation azimuths to improve signal quality for various data processing steps. Rotating to the fast and slow PS-wave directions can improve surface consistent deconvolution, surface consistent static corrections, and velocities. Rotating back to radial and transverse and processing common-azimuth volumes allowed all the data to be combined using 2Cx2C

rotation. This increased fold helped improve the signal quality, but only after azimuth-consistent static corrections were computed and applied.

Vps_{11}/Vps_{22} velocity ratio analysis is a valuable tool to quantify the vertical extent of S-wave birefringence as a function of time. As this ratio varies in time, it indicates different layers in the subsurface where birefringent properties may have changed. One of the most important of these layers is the overburden, which can be removed effectively by 2Cx2C rotation and layer-stripping analyses, and leads to quantifying the fracture properties at target horizons. Three analysis techniques (residual PS_{12} and PS_{21} amplitudes, PS_{11} and PS_{22} traveltime isochrons, and layer stripping) provide a broad range of interpretation tools and attributes that can help identify lateral variations in fracture properties.

Acknowledgments

We thank Jonathan Fried and John Young at WesternGeco for their help in processing the converted-wave data for this study. Thanks also to EOG Resources, Tom Brown Inc., and Stone Energy for their participation and for providing valuable insights into the nature of the reservoir.

References

Alford, R.M., 1986. Shear data in the presence of azimuthal anisotropy: Dilley, Texas. 56th Ann. Internat. Mtg., Soc. Expl. Geophys., Houston, Expanded Abstracts, 476-479.

Ata, E., and Michelena, R.J., 1995. Mapping distribution of fractures in a reservoir with P-S converted waves. *The Leading Edge*, **14**, 664-676.

Gaiser, J.E., 1999. Applications for vector coordinate systems of 3-D converted-wave data. *The Leading Edge*, **18**, 1290-1300.

Gaiser, J.E., Loinger, E., Lynn, H., and Vetri, L., 2001. PS wave velocity variations in azimuthally anisotropic media for layer stripping. 63rd EAGE Conf. and Tech. Exhibit., Amsterdam, Extended Abstract.

Grimm, R.E., Lynn, H.B., Bates, C.R., Phillips, D.R., Simon, K.M., and Beckham, W.E., 1999. Detection and analysis of naturally fractured gas reservoirs: multiazimuth seismic surveys in the Wind River basin. Wyoming. *Geophysics*, **64**, 1277-1292.

Winterstein D.F., and Meadows M.A., 1991. Shear-wave polarizations and subsurface stress directions at Lost Hills Field. Geophysics, **56**, 1331-1348.

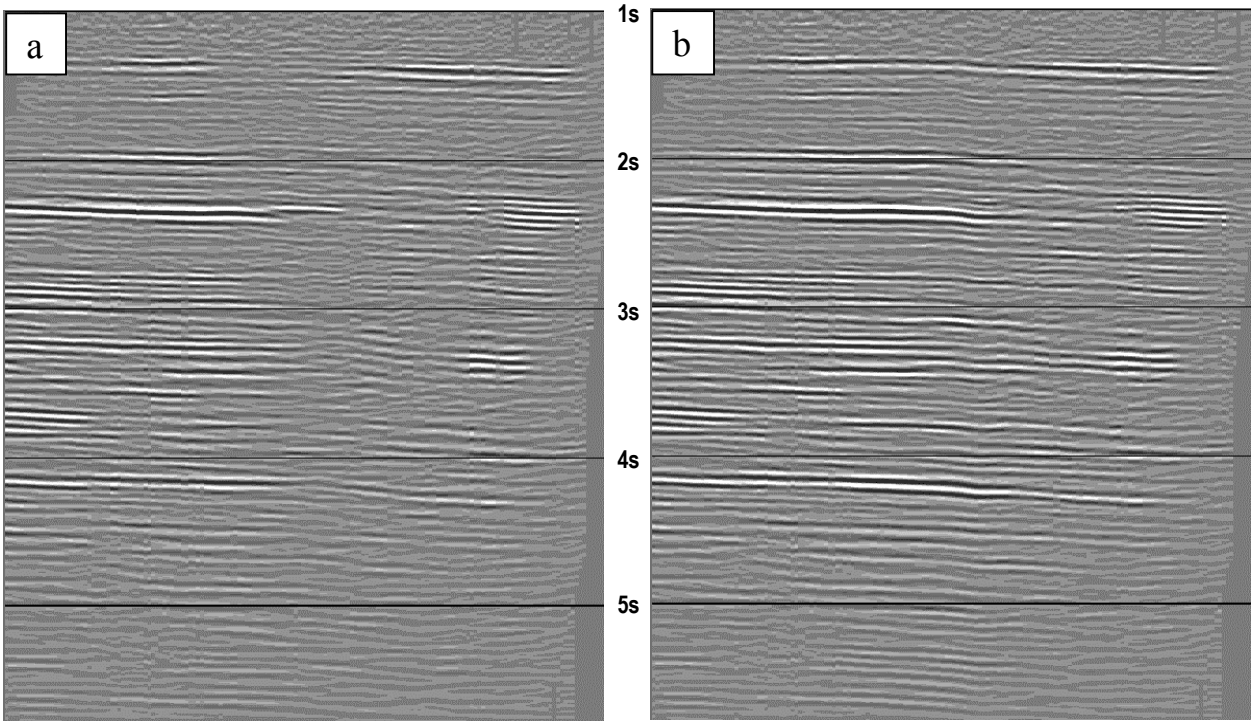

Figure 1. (a) Radial component stack of eight combined propagation azimuths after rotation to the principal PS_1 direction (N137°E). (b) Same stack with azimuth-consistent static corrections applied showing improved reflector continuity, particularly on the right half of the line.

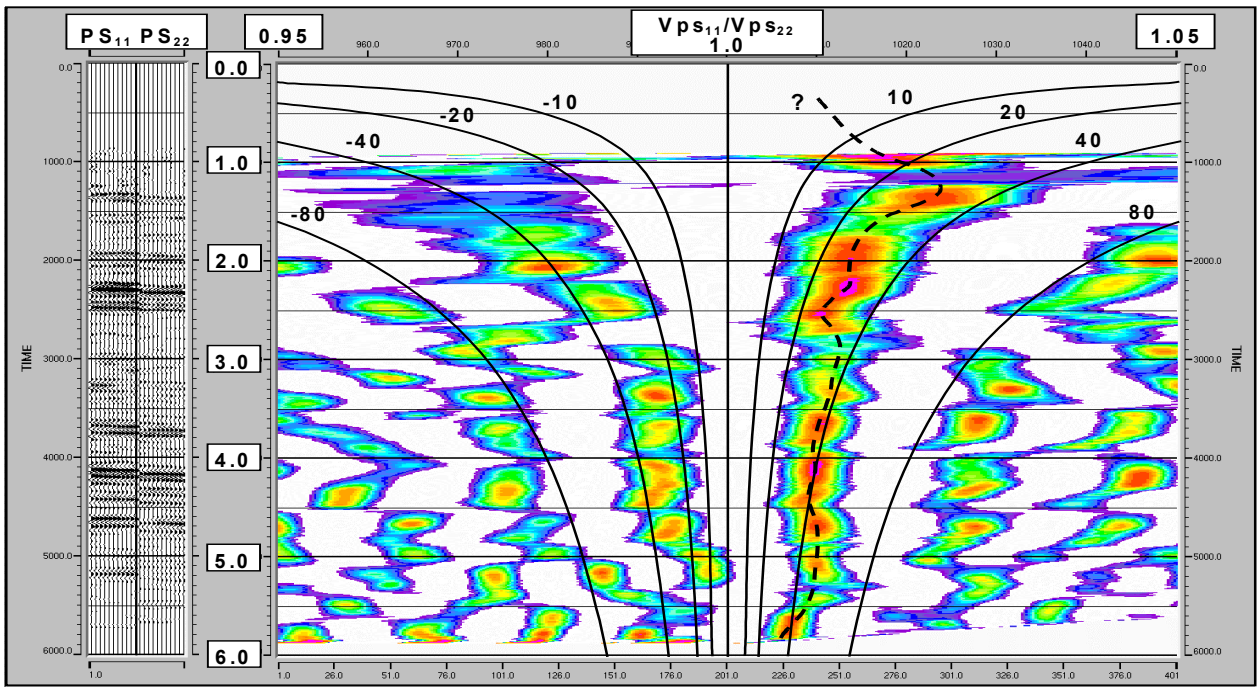

Figure 2. Average velocity-ratio analysis between the PS_{11} and PS_{22}.traces (left) located near the well in the northern part of the survey. The Vps_{11}/Vps_{22} ratio ranges from 0.95 to 1.05, time is two-way PS_{11}, and variable density represents positive cross-correlation coefficients between PS_{11} and PS_{22}. Contours indicate constant PS_{22} time delays and the dashed line shows the interpreted relationship between the split S-waves. The base of the overburden is interpreted at the maximum traveltime difference just below the event at 1.3 s.

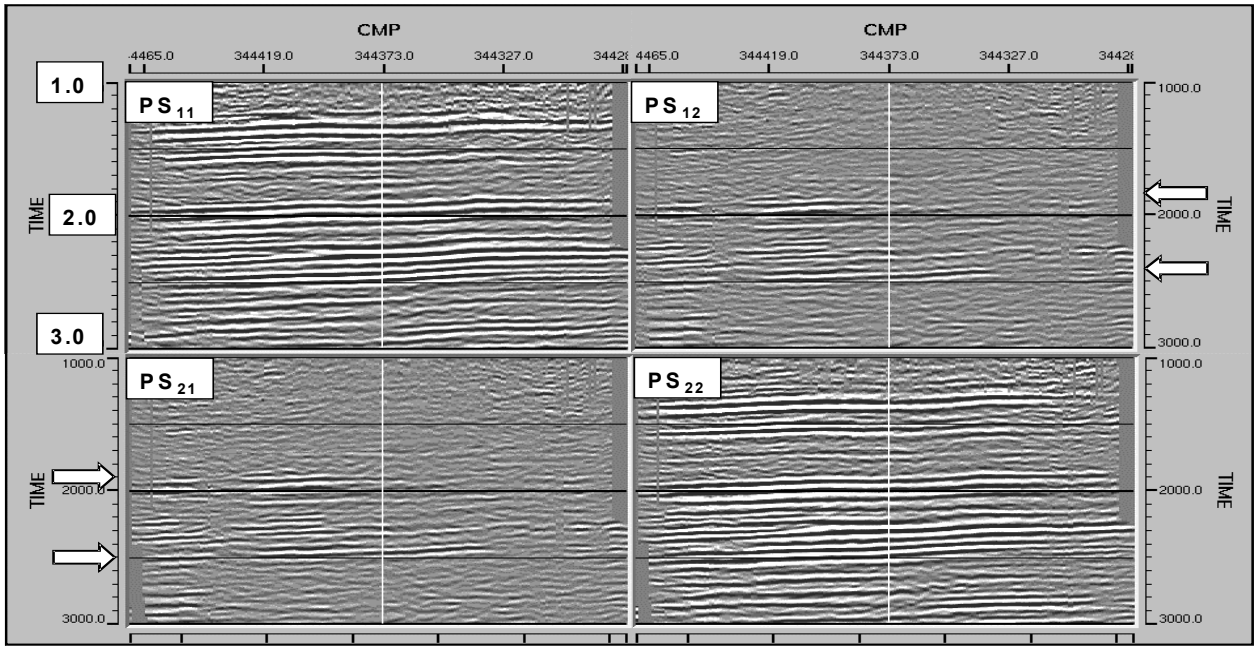

Figure 3. 2Cx2C inline section after Alford rotation and layer stripping the overburden. PS_{11} and PS_{22} are the principal components aligned through the overburden at about 1.6 s. These components are important for quantitative isochron analyses of percent azimuthal anisotropy. PS_{12} and PS_{21} are the off-diagonal components minimized through the overburden. Residual amplitudes below the overburden on PS_{12} and PS_{21} provide qualitative insights into changes in birefringence. The vertical white line indicates the location of the well and the Vps_{11}/Vps_{22} average velocity analysis in Figure 2.

Seismic Anisotropy in Trinidad: Processing and Interpretation

Tariq Alkhalifah, KACST, Saudi Arabia; and Dave Rampton, Shell oil Company, The Netherlands

Abstract

The imaging improvements are shown for two different lines from Trinidad. The lithology of offshore Trinidad is formed of alternating sequences of sand and shale dominated layers. Despite the presence of sands, accounting for anisotropy in seismic processing results in improved imaging of structural and stratigraphic features. Inversion for an interval value of the anisotropy parameter (η), suggests that low values are correlated with sands (or any other isotropic material), while high interval η values are correlated with shales. Correlation between separate independent measurements for η across common midpoints (CMPs) enhances the credibility of such estimates as a representation of real geologic parameters. The parameter η, which, if not zero, implies the existence of anisotropy, is used to discriminate conservatively between shales and sands. The underlying theory is that shales induce anisotropy, positive η in particular, and sands do not. Correlation of these η results with gamma-ray well-log measurements used as a shale estimate proves the credibility of the results.

Introduction

The discrimination between shales and sands in the subsurface is key to oil exploration. Reservoirs usually exist in sand layers, sandwiched between large columns of shale layers. Significant imaging improvement has been demonstrated using seismic processing that takes anisotropy into account (Alkhalifah , 1997a). Benefits include better focusing and positioning of fault plane images, as well as enhanced continuity of near horizontal stratigraphic reflections. This paper extends the analysis of anisotropic effects on seismic data to show the potential of using the inverted anisotropic parameter (η) to predict lithology. Correlation with gamma ray curves demonstrates the ability to estimate sand and shale dominated intervals in the subsurface using conventional P-wave streamer data.

Theory

Alkhalifah and Tsvankin (1995) demonstrated that, for transversely isotropic (TI) media with a vertical symmetry axis (VTI media), just *two* parameters are sufficient for performing all time-related processing such as NMO correction (including non-hyperbolic moveout correction, if necessary), DMO correction, and prestack and poststack time migration. One of these two parameters, η, is a dimensionless parameter, where its departure from zero implies anisotropy, and the other, $V_{\rm nmo}$, is the short-spread normal moveout (NMO) velocity for horizontal reflectors. These two parameters can be obtained solely from surface seismic P-wave data, using estimates of stacking velocity for reflections from interfaces having two distinct dips (Alkhalifah and Tsvankin, 1995). Alkhalifah (1997b) showed that these two parameters can also be obtained by analyzing the moveout at far offsets.

The Trinidad data

The first line of seismic data used in this abstract was acquired as a 2-D line in 1984 in the regional dip direction. The maximum offset acquired, 3200 m, is lower than what is typically acquired nowadays. Such offsets, nevertheless, are sufficient for applying the dip-moveout inversion of Alkhalifah (1997a) since this method does not require long offsets.

The second line of data from the Trinidad region is newer data (acquired in 1989), with offsets that extend to 6 km. This 2-D line was acquired in the regional subsurface dip direction. The source-to-receiver spacing ratio here is 3, and the maximum fold in the data is 90. Due to the large offsets acquired, a non-hyperbolic inversion (Alkhalifah, 1997b) is used on this data.

Anisotropy processing

The subsurface from offshore Trinidad contains reflections from a large number of dipping faults (see Figure 3). The section was processed using a conventional 2-D isotropic processing sequence that included a conventional NMO (using the stacking velocities that Amoco provided), followed by a log-stretch Fourier DMO. Anisotropy is expected to vary with depth due to the alternating sand-dominated and shale-dominated layers. Shales are believed to be the main source of anisotropy in sedimentary basins (Banik, 1984).

Carrying out the inversion process described

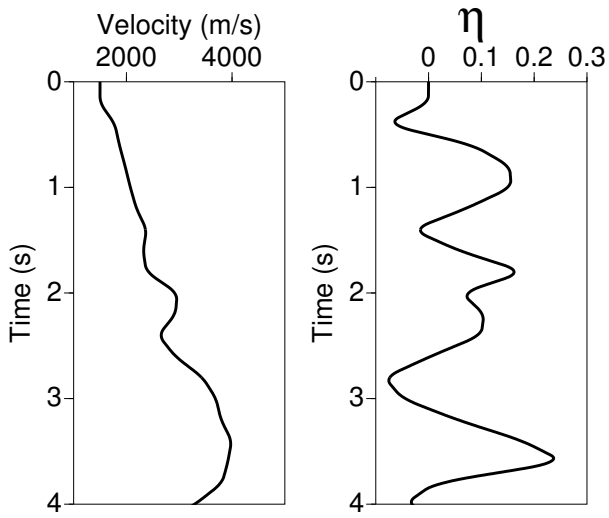

Figure 1: Estimated interval values v_{nmo} and η as a function of vertical time.

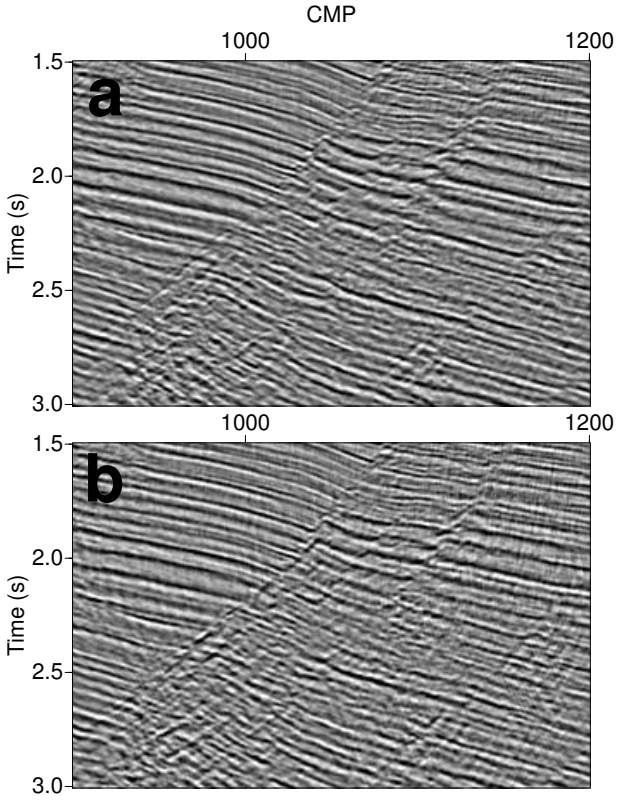

Figure 2: A detailed picture of Time-migrated sections of time-migrated sections after (a) isotropic processing, and (b) VTI processing.

by Alkhalifah (1997a), using the measured values of stacking velocities and corresponding ray parameters, we obtain the functions $v_{\text{nmo}}(\tau)$ and $\eta(\tau)$ shown in Figure 1. In the water layer, v_{nmo} is 1.5 km/s and η is zero. The accuracy of these estimated curves of v_{nmo} and η depends on the accuracy of the stacking-velocity estimates for both dipping and horizontal reflectors, as discussed by Alkhalifah and Tsvankin (1995).

The smoothed interval values of η in Figure 1 show variations that might depend on the shale-sand long-wavelength alterations. Specifically, shales are expected to induce anisotropic behavior (Banik, 1984) of waves, while sands are usually isotropic. The measurement that resulted in Figure 1 corresponds to the fault under CMP location 1100. Later we will examine results from other faults.

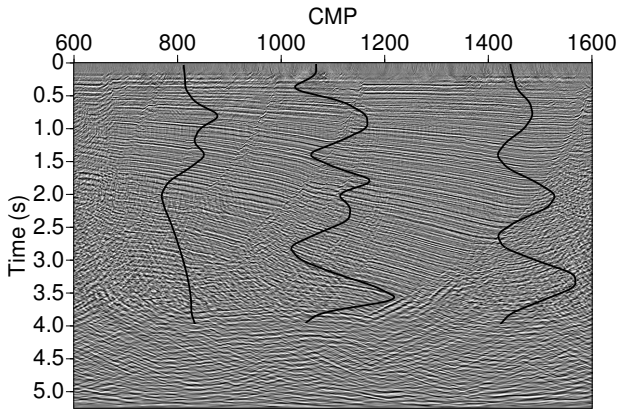

Figure 3: Three interval η curves superimposed on a VTI time-migrated section of the data. These values correspond to the region above each fault.

Next, we apply a DMO algorithm that uses the derived functions $v_{\text{nmo}}(\tau)$ and $\eta(\tau)$ followed by a TI migration. Figure 2 shows closeups of time-migrated sections after (a) isotropic processing, and (b) VTI processing using the inverted parameters shown in Figure 1. The figure clearly demonstrates the improved imaging achieved by considering anisotropy. Presence of fault plane reflections suggest that the fault is probably a potential reservoir seal. These reflections are typically attenuated and/or lost by isotropic processing, while anisotropic processing is successful at preserving these fault plane images.

Three large faults can be picked from this line. Independent estimates for interval η are made at each of these faults. Figure 3 shows the three inter-

val η curves super imposed on the full TI migrated section. Because the left most fault shows relatively little throw, the corresponding η curve lacks the detail evident in the other two curves, especially at depth. Note, the correlation between the three interval η curves agrees well with the continuity of seismic reflections across the section. The lateral correlation of interval η increases confidence that a geologic parameter is represented by the inversion. Correlation of interval η estimates across faults could help to remove ambiguity in determining correlation of seismic picks across a seismic section.

Parameter estimation

We, also, use the nonhyperbolic moveout inversion of Alkhalifah (1997b) to estimate interval η for another seismic line from Trinidad. The result of this inversion is an interval η curve as a function of time. This inversion, though based on a laterally homogeneous medium assumption, has some tolerance to lateral inhomogeneity, such as the lateral inhomogeneity associated with most faults.

This line also contains a large number of faults (see Figure 4). Wells are located at CMP 1100 and 1220; both above an anticline structure. Note that the data beyond 2.5 s are of poor quality.

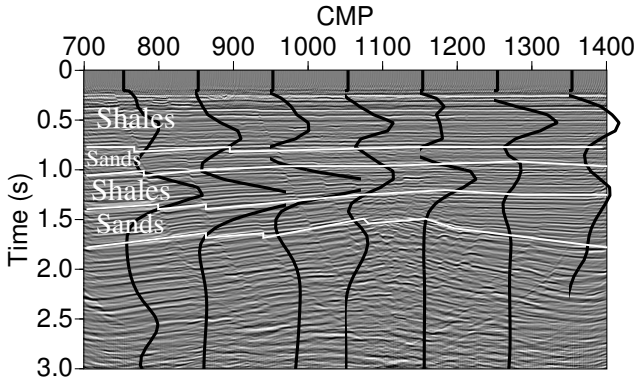

Figure 4: A lithological interpretation of the sand and shale content of the surface as estimated by the interval η values obtained from the inversion. The white lateral lines follow seismic reflections. The second sand layer may include respectable amounts of shale.

Figure 4 shows seven η curves superimposed on a migrated section from this region. These η curves are placed in their respective positions in Figure 4. The lateral correlation between these curves, which are about 1.25 km apart, is also remarkable. Especially remarkable is the correlation between the thickness of the shale layers and the size of η as we can see by comparing the measurements at CMP 750 with that at CMP 1050 for the top layer. Figure 4 also shows a crude lithologic interpretation estimated solely from the anisotropic inversion. The interpretation is based on the fact that shales are anisotropic, and therefore exhibit large positive η values, while sands are essentially isotropic with near-zero values of η. The second sand layer may also include a lot of shales because the drop in η is not very definite. Also, at this depth the data quality is bad.

A more continuous estimation of η is given by the 2-D plot of η in Figure 5 (at the bottom), where measurements were taken at practically every CMP location and subsequently used to estimate a more continuous interval η distribution. Figure 5 (at the top) shows the interval velocity extracted through the same process. Most of the observations regarding Figure 4 apply here as well. However, more detail is apparent in this continuous η representation. The three major faults in the area are drawn to show their effect on the measurements. The poor quality of data at later times is the reason behind the lack of estimates at depth.

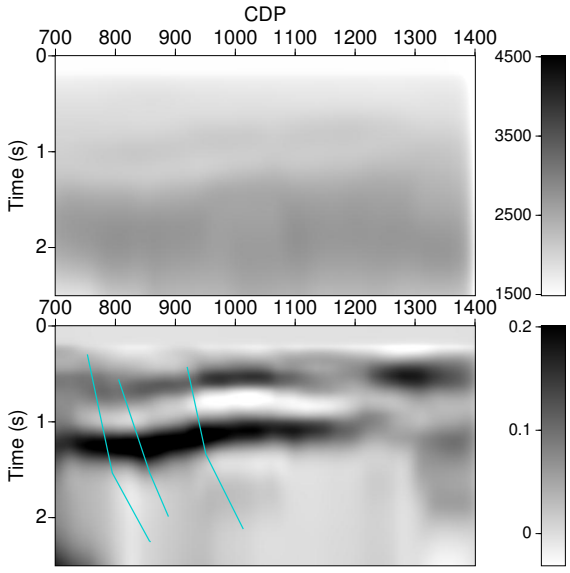

Figure 5: Top: the interval NMO velocity corresponding to the data in Figure 4. Bottom: interval η values for the same data.

Well control

To verify the preceding observations, Figure 6 compares the η curve with gamma ray logs available from nearby wells. The well location is at CMP 1100. The Gamma ray logs indicate the presence of sands just prior to the one second mark. At this time, the η curve also shows small values suggesting the this part of the vertical column is isotropic. Because shales induce anisotropy, more likely than not, this part of the section corresponds to sands. Figure 5 provides information from seismic data of the lateral extent of this sand layer, or layers. At this CMP location, the correlation between the well-log measurements, at a lower resolution, and the η curve is remarkable. Even correlation between the curves in Figure 6 can be made at the high-frequency end, where some of the spikes have the same time. Recall, that the η curve is obtained in its entirety from P-wave surface seismic data. Yet, information like the low-frequency character of the shale-sand content is extracted from these data.

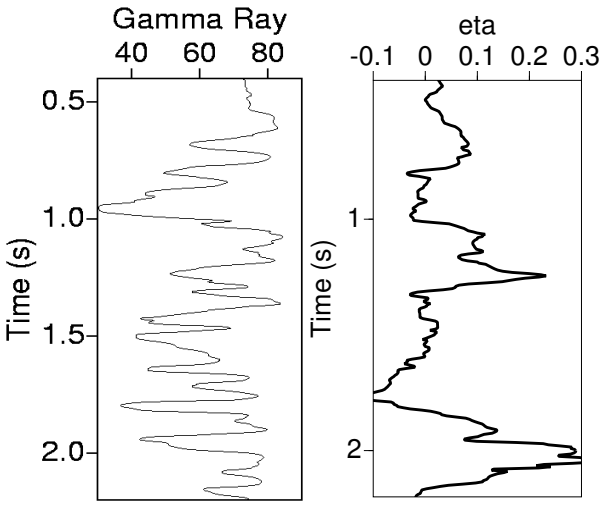

Figure 6: Left: Gamma ray logs from a well located at CMP location 1100 in Figure 3, smoothed using a conventional box function smoother with a window 50 feet's. Right: interval η values obtained from the seismic data for the same location.

Conclusion

By acknowledging the influence of anisotropy on seismic data, we have roughly estimated the anisotropic parameter η. This parameter, if accurately estimated, can be used to discriminate between shales and sands in the subsurface. Obtaining such information from surface seismic P-wave data has important implications for deep water surveys, where the cost of drilling wells is large. This technique does not require expensive or unusual acquisition procedures—the only requirement is a new look at existing data using refined processing techniques that incorporate real geologic parameters.

Acknowledgments

We thank Amoco Trinidad Oil Company for providing the data and their various assistance with the data.

Refrences

Alkhalifah, T., 1997a, Seismic Data Processing in vertically inhomogeneous TI media: Geophysics, **62**, 662-675.

Alkhalifah, T., 1997b, Velocity analysis using non-hyperbolic moveout in transversely isotropic media: Geophysics, in press.

Alkhalifah, T., and Tsvankin, I., 1995, Velocity analysis for transversely isotropic media: Geophysics, **60**, 1550-1566.

Banik, N. C., 1984, Velocity anisotropy of shales and depth estimation in the North Sea basin: Geophysics, **49**, 1411–1419.

Lynn, W., Gonzalez, A., and MacKay, S., 1991, Where are the fault-plane reflections?, 61st Ann. Internat. Mtg., Soc. Expl. Geophys., Expanded Abstracts, 1151–1154.

Stress-induced velocity anisotropy on Açu sandstone, Potiguar Basin, Brazil

José Agnelo Soares, Federal University of Rio de Janeiro, Brazil, agnelo@igeo.ufrj.br
Jorge Leonardo Martins, GTEP - Pontifical Catholic University of Rio de Janeiro, Brazil, jlm@civ.puc-rio.br
Jadir da Conceição da Silva, Federal University of Rio de Janeiro, Brazil, jadir@igeo.ufrj.br

Abstract

Rock samples from Açu sandstone, Potiguar Basin, Brazil, were submitted to measurements of P and S wave velocities. It was done under several conditions, combining application of constant confining pressure and increasing axial deviatoric stress, with simultaneous monitoring of both axial and transversal strains, that allows correction on rock density and elastic moduli. By using the appropriate model of stress-induced anisotropy for the data set obtained in the experiments, third-order elastic constants for the sandstone were estimated. These estimates, for each rock specimen, led to velocity modeling for the sandstone along arbitrary directions and different stress magnitudes. This procedure yielded the quantification of the velocity anisotropy on the Açu sandstone under the application of incremental stress fields.

Introduction

In this work it was used the solution of Hughes & Kelly (1953) for P and S wave velocities in an elastic medium under stress. Such solution includes the influence of static stresses on the propagation of elastic waves. Still, the mentioned solution takes into account the second-order stress-strain relationship instead of using the usual linear Hooke´s law. As a direct consequence of the stress application, more three [non-linear] elastic constants, *l*, *m* and *n*, are required to describe the anisotropic behavior of the isotropic material under stress, in addition to the Lamé constants λ and μ. The elastic constants, *l*, *m* and *n*, are termed here as Murnaghan´s constants, in reference to Murnaghan (1951). Conceptually, these are in fact third-order elastic constants in opposite to Lamé parameters, which are second-order elastic constants (Bentahar et al, 2000).

Hughes and Kelly (1953) presented expressions for P and S wave velocities for two cases of stress conditions. Both wave velocity expressions depend on pressure in the case of pure hydrostatic load, and on stress in the case of axial compressive load. Engelhard (1988) showed that the terms dependent on pressure and on stress could be added to express the general case of confining pressure plus deviatoric stress.

For pure hydrostatic pressure *p*, the equations for P and S wave velocities are given as follows

$$\rho_0 V_P^{\,2} = (\lambda + 2\mu) - \frac{p}{3K}(10\mu + 7\lambda + 6l + 4m)$$
$$\rho_0 V_S^{\,2} = \mu - \frac{p}{3K}\left[3(\lambda + 2\mu) + 3m - \frac{1}{2}n\right] \quad (1)$$

and for axial compressive stress σ parallel to the direction of wave propagation, equations evolve to

$$\rho_0 V_P^{\,2} = (\lambda + 2\mu) - \frac{\sigma}{3K}\left[\frac{\mu + \lambda}{\mu}(10\mu + 4\lambda + 4m) + \lambda + 2l\right]$$
$$\rho_0 V_S^{\,2} = \mu - \frac{\sigma}{3K}\left[4(\mu + \lambda) + \frac{\lambda}{4\mu}n + m\right] \quad (2)$$

In the equations above, V_P and V_S are P and S wave velocities, respectively, K is the bulk modulus and ρ_0 indicates the rock density in the underformed state.

The data used in this research for evaluation of Murnaghan´s parameters can be found in Araújo (1995), where thirteen Açu sandstone core samples were submitted to laboratory measurements. Figures 1 and 2 illustrate the stress-strain behavior of the studied rock specimens, each of which was subjected to a constant confining (hydrostatic) pressure and increasing axial deviatoric stresses up to rock failure. In addition to axial and radial strain measurements, V_P and V_S were recorded in the axial direction as well. In average, velocities were collected on five points for each test. In order to calculate Murnaghan´s parameters *l*, *m* and *n*, an appropriate combination of the previous equations, that takes into account the stress field on the rock samples, must be considered.

Murnaghan´s parameters

Let us insert the stress-dependent part of equations (2), for axial compression, into equations (1), for pure hydrostatic load (Engelhard, 1988). This leads to the complete set of equations that allow modeling both P and S wave velocities obtained in laboratory tests under the same stress conditions. This operation furnishes

$$\rho_0 V_P^{\,2} = (\lambda + 2\mu) - \frac{p}{3K}(10\mu + 7\lambda + 6l + 4m) - \frac{\sigma}{3K}\left[\frac{\mu + \lambda}{\mu}(10\mu + 4\lambda + 4m) + \lambda + 2l\right] \quad (3)$$

for P-wave velocities, and

$$\rho_0 V_S^{\,2} = \mu - \frac{p}{3K}\left[3(\lambda+2\mu)+3m-\frac{n}{2}\right] - \frac{\sigma}{3K}\left[4(\mu+\lambda)+\frac{\lambda}{4\mu}n+m\right] \quad (4)$$

for S-wave velocities. Note that *p* represents here the confining pressure, while σ stands for the deviatoric compressive stress.

After rearranging equations (3) and (4), the following linear relationships between the Murnaghan's constants are obtained

$$l = \frac{A}{\left(\frac{2p}{K}+\frac{2\sigma}{3K}\right)} + \frac{\left[\frac{-4\sigma}{3K}\left(\frac{\mu+\lambda}{\mu}\right)-\frac{4p}{3K}\right]}{\left(\frac{2p}{K}+\frac{2\sigma}{3K}\right)}m \quad (5)$$

and

$$m = \frac{B}{\left(\frac{p}{K}+\frac{\sigma}{3K}\right)} + \frac{\left(\frac{p}{6K}-\frac{\sigma\lambda}{12K\mu}\right)}{\left(\frac{p}{K}+\frac{\sigma}{3K}\right)}n \quad (6)$$

where

$$A = (\lambda+2\mu)-\rho_0 V_P^{\,2} - \frac{p}{3K}(10\mu+7\lambda) - \frac{\sigma}{3K}\left[\frac{\mu+\lambda}{\mu}(10\mu+4\lambda)+\lambda\right] \quad (7)$$

and

$$B = \mu - \rho_0 V_S^{\,2} - \frac{p}{K}(\lambda+2\mu) - \frac{4\sigma}{3K}(\mu+\lambda) \quad (8)$$

The use of the data set obtained from laboratory measurements on the samples of Açu sandstone, a set of linear equations can be constructed. The systems thus formed for each rock specimen were solved for the Murnaghan´s parameters. Figures 3 and 4 depict graphical solutions for Murnaghan´s parameters on rock sample AP-3. Note the unique solution for each Murnaghan´s parameter, which was determined independently of the differential deviatoric stress levels. This behavior clearly indicates that the determination of *l*, *m* and *n* parameters is insensitive to deviatoric stress changes. Table 1 shows the calculated values of *l*, *m* and *n* for all tested rock samples. Further, confining pressure, temperature and initial density ρ_0 are shown. All samples were fully saturated with mineral oil.

Velocity modeling

Simulation of P and S wave velocities under any condition of confining pressure and differential deviatoric stress can be performed. The data set required are: Murnaghan´s constants, rock density in the underformed state and Lamé constants as a function of pressure. In this work, we used the data listed in Table 1 for velocity modeling. The Murnaghan´s constants were estimated for several rock samples as described above. Bulk density ρ_0, as well as fitting functions of Lamé constants versus applied stress were laboratory-acquired. Figure 5 illustrates fitting functions of shear modulus (μ) versus total stress for a subset of rock samples named AP.

Figures 6 to 9 depict the upper right quadrant of azimuthal P wave velocity anisotropy due to an arbitrary horizontal deviatoric stress of 90° of azimuth, for some laboratory-tested rock samples from Açu sandstone showed in Table 1. In these figures, inner curve in black represents P wave velocity for the *isotropic* rock sample, *i.e.*, without deviatoric stress application. Curves in green, blue and red indicate P wave velocities for three conditions of deviatoric stress application. Note that magnitudes of incremental stresses σ are, respectively, 20%, 60% and 100% of the magnitude of the confining pressure.

It can be observed the dependence of stress-induced anisotropy on the magnitude of the deviatoric stress. Let the P-wave velocity anisotropy be defined as the percentual increment of velocity in the parallel direction of the deviatoric stress in comparison with the velocity in the perpendicular direction. Bearing this definition in mind, an incremental deviatoric stress of 20% of the confining pressure caused nearly 2% of anisotropy. The increase of the deviatoric stress to 60% of the confining pressure caused a P-wave anisotropy around 5% to 6%. Approximately 7% to 10% in P-wave anisotropy was observed when the deviatoric stress reached 100% of the confining pressure.

Conclusions

Laboratory monitoring of P and S wave velocities on rock samples under several conditions of stress application allows calculation of the third-order elastic [Murnaghan's] parameters. By using Murnaghan's parameters, which are independent of any state of stress applied to the material, wave velocities under any stress condition can be predicted.

In the Açu sandstone, for arbitrary deviatoric stress magnitudes varying from 20% to 100% of confining pressure, stress induced anisotropy values of 2% to 10% were found. This result allows to characterize the anisotropy of the Açu sandstone as weak.

Acknowledgements

Thanks to PETROBRAS Rock Mechanics and Rock Physics Labs for sample preparation and facilities. Our gratitude to Marcos Leão for equipment assistance during velocity measurements and Lincoln Homero for acquisition software development. Jorge L. Martins acknowledges support from the Brazilian Council for the Development of Sci. & Tech, CNPq/RHAE, under process no. 610154/99-0.

References

Araújo, R. G. S. ,1995, Determinação da influência da temperatura nos parâmetros elásticos e de resistência em rochas reservatório de petróleo. Dissertação de mestrado. FEM / UNICAMP. (*In Portuguese*).

Bentahar, M., Badidi-Bouda, A., and Benchaala, A., 2000, Second and third-order elastic constants determination of an isotropic metal, 15th World Conf. on Non-Destructive Testing, 15-21/October, Rome, Italy.

Engelhard, L., 1988, Stress-induced anisotropy in elastic media. Geophysical Transactions, 34, 59-81.

Hughes, D. S., and Kelly, J. L., 1953, Second-order elastic deformation of solids. Physical Review, 92, 1145-1149.

Murnaghan, F. D., 1951, Finite deformation of an elastic solid. J. Wiley, New York.

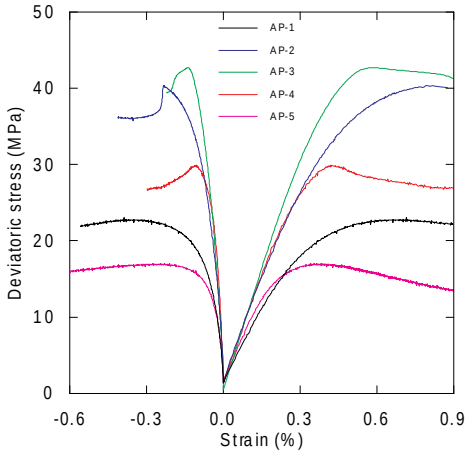

Figure 1 – Stress-strain curves for AP samples.

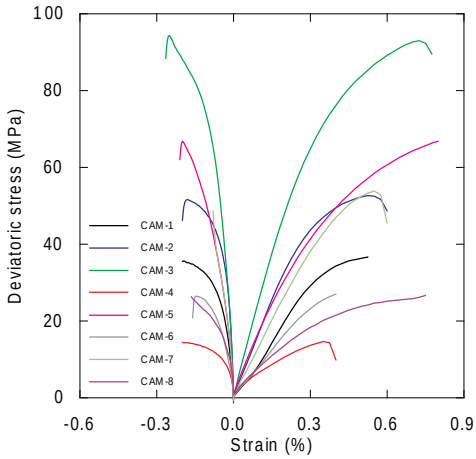

Figure 2 – Stress-strain curves for CAM samples.

Table 1 – Murnaghan´s parameters.

sample	P (MPa)	Temp. (°C)	ρ_0 (Kg/m³)	*l* (GPa)	*m* (GPa)	*n* (GPa)
AP-1	7.5	150	2073	+10	-21	-80
AP-2	20	150	2093	+2	-22	-66
AP-3	15	25	2169	-10	-28	-50
AP-4	7.5	150	2103	-4	-21	-50
AP-5	2.5	25	2105	+39	-27	-95
CAM-1	5	25	2283	+37	-38	-150
CAM-2	7.5	80	2498	+20	-50	-165
CAM-3	15	150	2532	+5	-60	-155
CAM-4	10	160	2410	+4	-26	-65
CAM-5	20	80	2418	-20	-41	-44
CAM-6	5	80	2230	+12	-31	-105
CAM-7	10	25	2347	-16	-37	-40
CAM-8	10	80	2203	-6	-20	-37

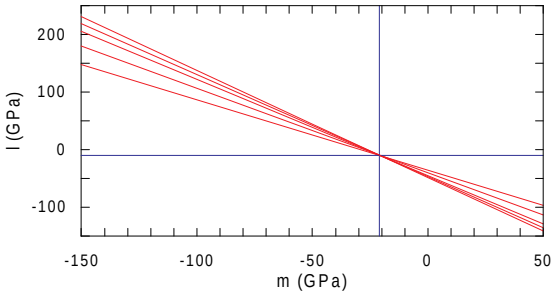

Figure 3 – Solution for *l* and *m* in sample AP-3.

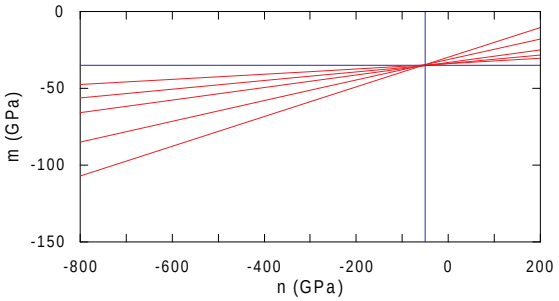

Figure 4 – Solution for *m* and *n* in sample AP-3.

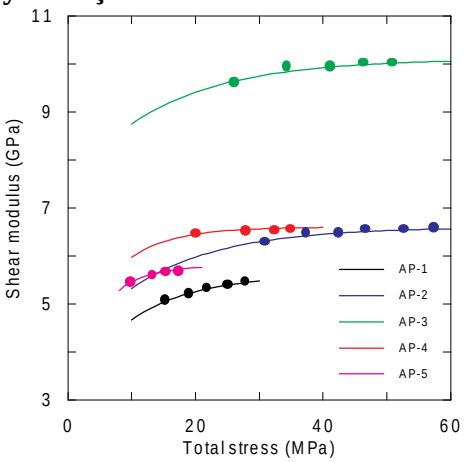

Figure 5 – Fitting functions for μ in AP samples.

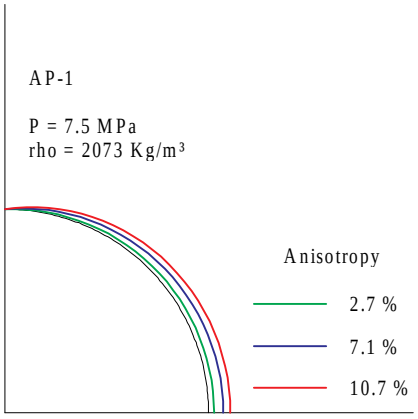

Figure 6 – Modeled P wave velocity on sample AP-1 due to deviatoric horizontal stress of 1.5 MPa (green), 4.5 MPa (blue) and 7.5 MPa (red).

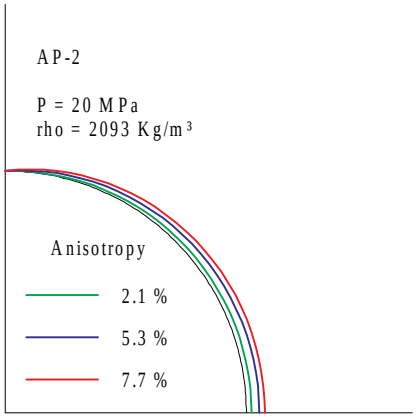

Figure 7 – Modeled P wave velocity on sample AP-2 due to deviatoric horizontal stress of 4 MPa (green), 12 MPa (blue) and 20 MPa (red).

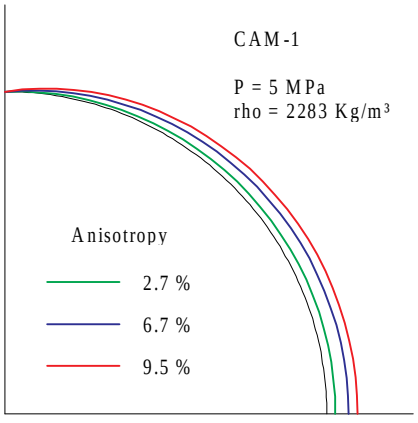

Figure 8 – Modeled P wave velocity on sample CAM-1 due to deviatoric horizontal stress of 1 MPa (green), 3 MPa (blue) and 5 MPa (red).

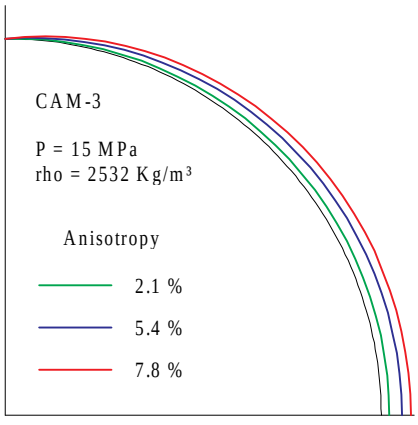

Figure 9 – Modeled P wave velocity on sample CAM-3 due to deviatoric horizontal stress of 3 MPa (green), 9 MPa (blue) and 15 MPa (red).

Uncertainty analysis for inversion of qP-wave reflection amplitudes in weakly anisotropic elastic media

Jorge Leonardo Martins, GTEP/PUC-Rio, Brazil, jlm@civ.puc-rio.br

Ivan Pšenčík, Geophysical Inst., Acad. of Sci. of Czech Republic, Czech Republic, ip@ig.cas.cz

Abstract

An approximate equation for $qPqP$ reflection coefficients is used in order to recover contrasts in weak anisotropy (WA) parameters of media surrounding an interface. The approximation fits, within the subcritical region, exact calculations of reflections at a weak-contrast interface separating two homogenous, weakly anisotropic elastic media of arbitrary symmetry. Linear dependence of reflection amplitudes on contrasts in WA parameters is convenient property of this approximation. Hence, the singular value decomposition (SVD) technique is applied to recovering the contrasts, with numerical reflection data from an interface separating an upper isotropic halfspace from a bottom transversely isotropic halfspace with horizontal axis of symmetry (HTI). Reflection amplitudes from a range of incidence angles commonly found in practice and from at least five measurement profiles are needed for recovering the contrasts in WA parameters. Such a conclusion is drawn by performing an uncertainty analysis for the inversion.

Introduction

Amplitude versus offset (AVO) analysis is a powerful tool for lithology characterization and fluid content prediction (Smith and Gidlow, 1987). Due to the fact that seismic anisotropy represents an inherent phenomenon in sedimentary sequences (Winterstein and De, 2001), there is a need for performing AVO analysis along specific directions in which amplitude anomalies may be higher. Bearing this in mind, such a technology is referred to as amplitude versus direction (AVD) analysis (MacBeth and Li, 1999).

The use of approximations for reflection coefficients is the fundamental part in AVO/AVD studies. In isotropic AVO analysis, various modifications of the approximate formula for PP reflections derived in Aki and Richards (1980) is widespreadly used. Ignoring anisotropic effects in sedimentary rocks may lead to erroneous predictions (Wright, 1987). It is the case, for instance, if a vertically fractured reservoir rock is under investigation (Rüger and Tsvankin, 1997). An isotropic AVO analysis will work satisfactorily along the plane of fractures (i.e., the plane of isotropy). On the other hand, anisotropic effects due to the vertical fractures must be considered along the strike direction. This aspect explains the need for incorporating effects of azimuthal anisotropy in AVO studies.

Several approximations for $qPqP$ reflections have been proposed so far. The common assumption among them is the weak anisotropy behavior, which is inherent to most sedimentary formations (Thomsen, 1986). The assumptions of weak contrast across interfaces and weak anisotropy lead to simplification of exact expressions for reflections in anisotropic media.

Basically, the linearized coefficients are written as a sum of the approximation for reflections in the background isotropic media and a correction to weak anisotropy. Approximate equations are mostly restricted to transversely isotropic media with vertical axis of symmetry (Banik, 1987; Thomsen, 1993) or with horizontal axis of symmetry (Rüger, 1997). Approximations in orthorhombic media were studied by Rüger (1998), but only within symmetry planes. A common point in these approximations is the use of both vertical P and S wave velocities for the derivation of the equation for the coefficients. In this contribution, an approximation for $qPqP$ reflections in weakly anisotropic media studied by Pšenčík and Martins (2001) is used for inversion purposes. The approximation holds for arbitrary anisotropic symmetries and for arbitrary background isotropic velocities. For completeness of inversion, uncertainty analysis is implemented according to the same guidelines followed by Cai and McMechan (1999).

The linearized anisotropic reflections

The approximation for the $qPqP$ reflection coefficients used in this numerical study has the following form

$$R_{PP}(\varphi,\theta) = R_{PP}^{iso}(\theta) + \Delta R_{PP}(\varphi,\theta), \qquad (1)$$

where $R_{PP}^{iso}(\theta)$ is the well-known approximate formula for reflections at a weak-contrast interface separating two isotropic media (Aki and Richards, 1980) and

$$\begin{aligned}\Delta R_{PP}(\varphi,\theta) = {} & A\cos^2\theta + B_1\cos^2\varphi\sin^2\theta \\ & + B_2\sin^2\varphi\sin^2\theta + B_3\sin\varphi\cos\varphi\sin^2\theta \\ & + C_1^4\varphi\cos\varphi\sin^2\theta\tan^2\theta + C_2\sin^4\varphi\sin^2\theta\tan^2\theta \\ & + C_3\cos^2\varphi\sin^2\varphi\sin^2\theta\tan^2\theta \\ & + C_4\cos^3\varphi\sin\varphi\sin^2\theta\tan^2\theta \\ & + C_5\cos^3\varphi\cos\varphi\sin^2\theta\tan^2\theta, \qquad (2)\end{aligned}$$

represents the first-order perturbation from isotropy to weak anisotropy. To simplify notation, the subscript PP is used henceforth in place of $qPqP$.

The approximation in Eqs. (1) and (2) is linearized version of Eq. (39) of Vavryčuk and Pšenčík (1998). Its dependence on the incidence angle θ and on the direction of the measurement profile (azimuth) φ is clearly observed. Moreover, Eq. (2) explicitly shows *linear* dependence of reflections on constrasts in WA parameters across interface,

$$A = \frac{1}{2}\,\Delta\epsilon_z, \qquad B_1 = \frac{1}{2}\left[\Delta\delta_x - 8\left(\frac{\bar\beta}{\bar\alpha}\right)^2 \Delta\gamma_x\right],$$

$$B_2 = \frac{1}{2}\left[\Delta\delta_y - 8\left(\frac{\bar\beta}{\bar\alpha}\right)^2 \Delta\gamma_y\right], \qquad (3)$$

$$B_3 = \left[\Delta\chi_z - 4\left(\frac{\bar\beta}{\bar\alpha}\right)^2 \Delta\epsilon_{45}\right], \quad C_1 = \frac{1}{2}\,\Delta\epsilon_x,$$

$$C_2 = \frac{1}{2}\,\Delta\epsilon_y, \quad C_3 = \frac{1}{2}\,\Delta\delta_z, \quad C_4 = \Delta\epsilon_{16}, \quad C_5 = \Delta\epsilon_{26}.$$

The presence of R_{PP}^{iso} in Eq. (1) and the relationships in (3) also indicate dependence of reflections on upper

$$\alpha_1 = 2.260\ km/s$$
$$\beta_1 = 1.430\ km/s$$
$$\rho_1 = 2.700\ g/cm^3$$

$$\begin{pmatrix} 5.00 & 1.82 & 1.82 & 0.00 & 0.00 & 0.00 \\ & 6.25 & 1.75 & 0.00 & 0.00 & 0.00 \\ & & 6.25 & 0.00 & 0.00 & 0.00 \\ & & & 2.25 & 0.00 & 0.00 \\ & & & & 1.87 & 0.00 \\ & & & & & 1.87 \end{pmatrix}$$

$$\alpha_2 = 2.500\ km/s \qquad \beta_2 = 1.500\ km/s \qquad \rho_2 = 2.700\ g/cm^3$$

$$\Delta\alpha/\bar\alpha = 0.101 \qquad \Delta\beta/\bar\beta = 0.048 \qquad \Delta\rho/\bar\rho = 0.000$$

Figure 1: The IH model corresponding of an isotropic medium over a vertically fractured (HTI) material. Upper and lower elastic parameters indicate weak contrast across the interface. The [weak anisotropy] HTI medium is defined by the matrix of density-normalized elastic parameters in km^2/s^2.

and lower background isotropic media, which are represented by α and β (P and S wave phase velocities, respectively). Contrasts across the interface are denoted by Δ (for example, density contrast: $\Delta\rho = \rho_2 - \rho_1$), and averages by a bar over the corresponding quantity. Subscripts 1 and 2 index upper and lower medium, respectively. We can see from Eq. (3) that the reflection coefficient (1) also depends on nine P-wave WA parameters (Pšenčík and Gajewski, 1998)

$$\delta_x = \frac{A_{13} + 2A_{55} - \alpha^2}{\alpha^2}, \quad \delta_y = \frac{A_{23} + 2A_{44} - \alpha^2}{\alpha^2},$$

$$\delta_z = \frac{A_{12} + 2A_{66} - \alpha^2}{\alpha^2}, \quad \epsilon_{16} = \frac{A_{16}}{\alpha^2},$$

$$\epsilon_{26} = \frac{A_{26}}{\alpha^2}, \quad \chi_z = \frac{A_{36} + 2\,A_{45}}{\alpha^2},$$

$$\epsilon_x = \frac{A_{11} - \alpha^2}{2\alpha^2}, \quad \epsilon_y = \frac{A_{22} - \alpha^2}{2\alpha^2}, \quad \epsilon_z = \frac{A_{33} - \alpha^2}{2\alpha^2},$$

and on three S-wave WA parameters

$$\gamma_x = \frac{A_{55} - \beta^2}{2\beta^2}, \quad \gamma_y = \frac{A_{44} - \beta^2}{2\beta^2}, \quad \Delta\epsilon_{45} = \frac{A_{45}}{\beta^2}.$$

WA parameters are generalizations of anisotropy parameters introduced by Thomsen (1986). As "observed" data for the inversion for contrasts in WA parameters (see below), reflection coefficients were calculated for the model proposed by Rüger (1997), see Figure 1. Exact and approximate reflections determined along three azimuths are shown in Figure 2. Although anisotropy is weak for this model, reflections vary significantly along azimuths.

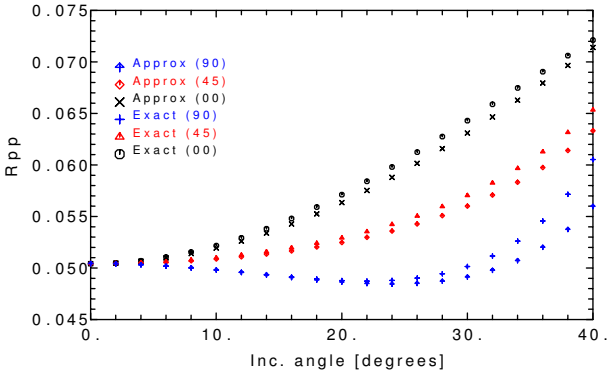

Figure 2: Exact and approximate reflection coefficients for the IH model in Figure 1. Approximate coefficients were calculated by using Eq. (1).

The inverse problem formulation

For a given data set of m observations, Eq. (2) represents a linear system for n sought parameters. The system can be written in matrix form as

$$\delta\mathbf{r} = \mathbf{L}\ \delta\mathbf{w}, \qquad (4)$$

where $\delta\mathbf{r}$ is a vector of differences of observed reflection coefficients $R_{PP}(\varphi,\theta)$ and coefficients $R_{PP}^{iso}(\theta)$. Each observation contributes to one equation in (4).

The elements of matrix $\mathbf{L}$ in Eq. (4) can be easily obtained from Eq. (2), i.e.

$$l_{i,1} = \cos^2\theta, \quad l_{i,2} = \cos^2\varphi\,\sin^2\theta, \quad l_{i,3} = \sin^2\varphi\,\sin^2\theta,$$

$$l_{i,4} = \sin\varphi\,\cos\varphi\,\sin^2\theta, \quad l_{i,5} = \cos^4\varphi\,\sin^2\theta\,\tan^2\theta,$$
$$l_{i,6} = \sin^4\varphi\,\sin^2\theta\,\tan^2\theta,$$
$$l_{i,7} = \cos^2\varphi\,\sin^2\varphi\,\sin^2\theta\,\tan^2\theta, \qquad (5)$$
$$l_{i,8} = \cos^3\varphi\,\sin\varphi\,\sin^2\theta\,\tan^2\theta,$$
$$l_{i,9} = \sin^3\varphi\,\cos\varphi\,\sin^2\theta\,\tan^2\theta.$$

Hence, $n = 9$ is the number of unknowns [Eqs. (3)] to be inverted, which are the elements of vector

$$\delta\mathbf{w} = (\,A \quad B_1 \quad B_2 \quad B_3 \quad C_1 \quad C_2 \quad C_3 \quad C_4 \quad C_5\,)^T. \qquad (6)$$

As a consequence of the configuration-dependence feature of the matrix $\mathbf{L}$, there should be a *minimum number of profiles* to be considered in the inversion so as to achieve a unique solution. Note that unknowns B_1, B_2 and B_3 are, in fact, combinations of contrast of two WA parameters.

Uncertainty analysis for the IH model

The model in Figure 1 was used for calculating exact reflection coefficients at each 2^o, in order to perform an iterative SVD inversion for contrasts in WA parameters according to the formulation described above. Velocities and the density of the isotropic medium in the upper halfspace were assumed to be known. Velocities

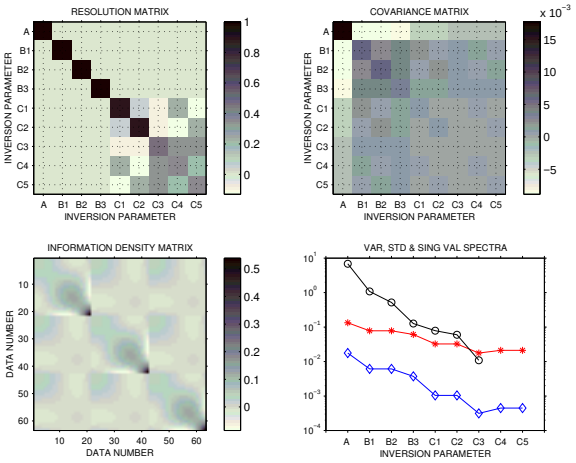

Figure 3: Uncertainty analysis for inversion of noise-free reflection coefficients with incidence information from 0^o to 40^o along three azimuths ($30^o/45^o/60^o$). Symbols $\diamond$, $*$ and $\circ$ denote variance, standard deviation and singular value, respectively.

of the background isotropic medium in the lower halfspace were iteratively updated during the process of inversion. The iterative process was stopped when the differences $\delta\mathbf{r}$ on the LHS of Eq. (4) were less than a predefined constant. The density of the lower halfspace was assumed to be known.

Two noise-free data sets were used for inversion. The first data set was obtained along three azimuths; the other data set gathered reflections from five azimuths. Both data sets contained incidence angles ranging from 0^o to 40^o. An inversion procedure is considered incomplete without performing an uncertainty analysis (Wiggins, 1972). Hence, we followed the same guidelines as in Cai and McMechan (1999) to analyse the resolution of the inversions.

The results of the uncertainty analysis for both inversions are shown in Figures 3 and 4. The resolution matrix is a measure of uniqueness of the solution; if the diagonal elements are units, the solution is said to be unique and the elements of the vector of sought parameters are said to be well resolved. The covariance matrix measures the uncertainty of the solution estimate. Its diagonal elements are variances, i.e., measures of uncertainty; if individual sought parameters have the same variance, they are said to be interdependent. The information density matrix is a measure of interdependence of the data used in the inversion. This matrix has zeros in all off-diagonal positions if each data observation is independent of all others. The more the information density matrix approaches a diagonal matrix, the more independent the observations.

By analysing Figures 3 and 4, the resolution matrices show that at least five measurement profiles

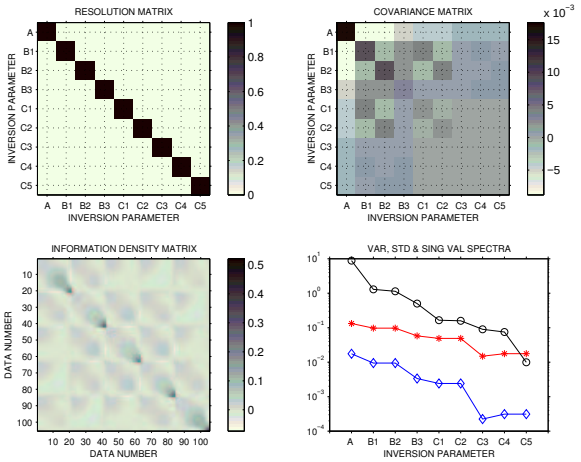

Figure 4: Uncertainty analysis for inversion of noise-free reflection coefficients with incidence information from 0^o to 40^o along five azimuths ($0^o/30^o/45^o/60^o/90^o$). Symbols $\diamond$, $*$ and $\circ$ denote variance, standard deviation and singular value, respectively.

are needed for a satisfactory estimation of contrasts in WA parameters. The data are highly interdependent, since the information density matrices exhibit off-diagonal trends. Interdependence of some unknowns (i.e., estimated contrasts) is observed in the covariance matrix plot. The curve of variances shows interdependence of contrasts B_1 and B_2, C_1 and C_2, and C_4 and C_5. The contrasts controlled by the *critical* term $\sin^2\theta\,\tan^2\theta$ in Eq. (1) are poorly resolved. This follows from the analysis of the singular values, see Figures 3

and 4. As can be seen in Figure 3, small singular values were neglected.

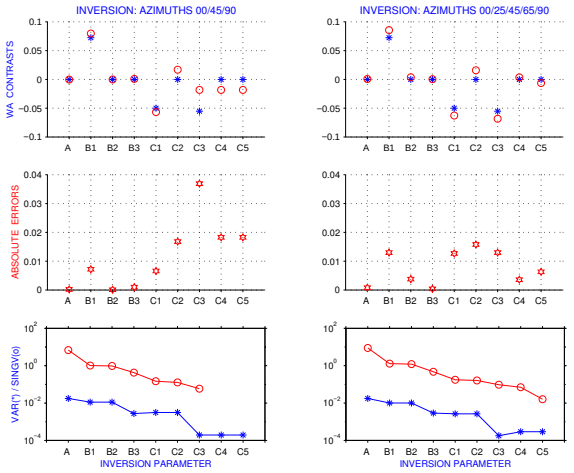

Figure 5: Outcomes from inversion of noise-corrupted reflection amplitudes using three ($0^o/45^o/90^o$) and five ($0^o/25^o/45^o/65^o/90^o$) profiles. Data with incidence information from 0^o to 40^o have been used for inversion. Upper plots show actual ($*$) and estimated ($\circ$) contrasts in WA parameters.

Gaussian noise ($\mu = 2.5 \times 10^{-3}$ and $\sigma = 7.5 \times 10^{-4}$) was added to exact reflection coefficients from the two previous experiments. In Figure 5 the confidence on the SVD inversion is analysed in terms of absolute errors, singular values and variances. Conclusions of previous inversions are confirmed.

Conclusions

Use of the approximation for reflections in weakly anisotropic media expressed in Eq. (1) allows a satisfactory estimation of contrasts in WA parameters even with noisy data. The inversion requires: (1) weak contrast and weak anisotropy for the media under study; (2) a priori information of background isotropic velocities, or at least an accurate estimation for those quantities; and (3) reflection data from offsets usually found in practice and from at least five measurement profiles. Under these assumptions, even small offset information can lead to estimation of important contrasts in WA parameters (i.e., B_1, B_2 and B_3).

Acknowledgments

The authors express their gratitude for the consortium project "*Seismic Waves in Complex 3-D Structures* (SW3D)", Czech Republic. Jorge L. Martins acknowledges support from ANP (proc. 48610.002779/99-31) and from CNPq/RHAE (proc. 610154/99-0). This abstract was prepared at GTEP - Group of Tech. and Petroleum Engineering, PUC-Rio.

References

Aki, K. I., and Richards, P. G., 1980. Quantitative Seismology: Theory and Methods. W. H. Freeman and Co., San Francisco, Vol. **I**, p. 153.

Cai, J., and McMechan, G. A., 1999, 2-D ray-based tomography for velocity, layer shape, and attenuation from GPR data. Geophysics, **64**, 1579–1593.

Banik, N. C., 1987. An effective anisotropy parameter in transversely isotropic media. Geophysics, **52**, 1654–1664.

MacBeth, C., and Li, X-Y, 1999. AVD - An emerging new marine technology for reservoir characterization: Acquisition and application. Geophysics, **64**, 1153–1159.

Pšenčík, I., and Gajewski, D., 1998. Polarization, phase velocity and NMO velocity of qP waves in arbitrary weakly anisotropic media. Geophysics, **63**, 1754–1766.

Pšenčík, I., and Martins, J. L., 2001. Properties of weak contrast PP reflection/transmission coefficients for weakly anisotropic elastic media. Studia Geophys. et Geod., **45**, 176-199.

Rüger, A., 1997. P-wave reflection coefficients for transversely isotropic models with vertical and horizontal axis of symmetry. Geophysics, **62**, 713–722.

Rüger, A., 1998. Variation of P-wave reflectivity with offset and azimuth in anisotropic media. Geophysics, **63**, 935–947.

Rüger, A., and Tsvankin, I., 1997. Using AVO for fracture detection: analytic basis and practical solution. The Leading Edge, **16**, 1429–1438.

Smith, G. C., and Gidlow, P. M., 1987. Weighted stacking for rock property estimation and detection of gas. Geophys. Prosp., **35**, 993–1014.

Thomsen, L., 1986. Weak elastic anisotropy. Geophysics, **51**, 1954–1966.

Thomsen, L., 1993. Weak anisotropic reflections. *In:* Offset-dependent reflectivity - theory and practice of AVO analysis, Castagna, J. P., and Backus, M. M., Eds., Investigations in Geophysics no. **8**, 103–111.

Vavryčuk, V., and Pšenčík, I., 1998. PP wave reflection coefficients in weakly anisotropic media. Geophysics, **63**, 2129–2141.

Wiggins, R. A., 1972. The general linear inverse problem: Implication of surface waves and free oscillations for earth structure. Rev. of Geophys. Space Phys., **10**, 251–285.

Winterstein, D. F., and De, G. S., 2001. VTI documented. Geophysics, **66**, 237–245.

Wright, J., 1987. The effects of transverse isotropy on reflection amplitude versus offset. Geophysics, **52**, 564–567.